minerals

MDPI

Article

Genetic Mechanism of Structurally Controlled Dolomites Derived from Seawater-Hydrothermal Mixed Fluids—A Case Study from Middle Permian, Central Sichuan Basin, South China

Jinliang Gao [1], Haofu Zheng [2,*], Bo Liu [3], Lei Pan [4], Rangbin Li [4], Junfeng Wu [2], Xiangyang Yang [2], Hailei Tang [5] and Yixin Dong [6]

[1] PetroChina Research Institute of Petroleum Exploration and Development, Beijing 100083, China; jinliang0205@126.com
[2] College of River and Ocean Engineering, Chongqing Jiaotong University, Chongqing 400074, China; wujunfeng@mails.cqjtu.edu.cn (J.W.); yangxy@cqjtu.edu.cn (X.Y.)
[3] School of Earth and Space Sciences, Peking University, Beijing 100871, China; bobliu@pku.edu.cn
[4] SINOPEC Exploration Company, Chengdu 610041, China; panl.ktnf@sinopec.com (L.P.); lirb.ktnf@sinopec.com (R.L.)
[5] Institute of International Rivers and Eco-Security, Yunnan University, Kunming 650500, China; highlytang@yeah.net
[6] State Key Laboratory of Oil and Gas Reservoir Geology and Exploitation, Chengdu University of Technology, Chengdu 610059, China; dongyixin008@hotmail.com
* Correspondence: zhenghaofu@cqjtu.edu.cn; Tel.: +86-18990017456

Abstract: Dolomite bodies in the Middle Permian of the central Sichuan Basin have been reported as favorable natural gas reservoirs. The Middle Permian dolomite consists of three types of recrystallized dolomite (Rd1, Rd2, and Rd3) and one type of dolomite cement (Sd). Rd1 might be formed as the primary mineral along the calcite in the original sea-water. Its $\delta^{13}C$ value and $^{87}Sr/^{86}Sr$ ratio, consistent with those of marine limestone and Permian seawater, support that the dolomitizing fluid for Rd1 was Permian seawater preserved in the strata. Rd2 consists of fine to medium (50 μm to 250 μm) and planar to curved crystals. Geochemical indicators (slightly high $^{87}Sr/^{86}Sr$ ratio, similar rare earth element patterns, negative $\delta^{18}O$, slightly high salinity) confirm that the dolomitizing fluid of Rd2 was mainly Permian seawater during shallow burial, with a small number of hydrothermal fluids. Rd3 and Sd are featured by very large (>250 μm), curved crystals, and high-temperature, high-salinity, and obviously positive Eu anomalies, suggesting that their diagenetic fluids were mainly hydrothermal fluids from deep. Additionally, inherited carbon sources and the $^{87}Sr/^{86}Sr$ ratios of some samples fall within the range of Permian seawater distribution, confirming the contribution of Permian seawater. ELIP activity caused the formation of this dolomite through the mixing of seawater and hydrothermal fluids. The main fluid circulation channels were activated basement faults, epigenetic karst pores, and shallowly buried high-permeability strata. During the peak period of ELIP activity, the continuous upwelling of deep hydrothermal fluids led to the continuous formation of Rd2, Rd3, and Sd. The dolomitization fluid of Rd2 was mainly composed of seawater and featured a certain lateral extension, which was away from faults. Rd3 and Sd are mainly distributed along the fault system, and excessive dolomitization caused by the hydrothermal activity, to some extent, inhibited the lateral movement of hydrothermal fluids. This study provides a good example for exploring the genetic mechanism and distribution pattern of structurally controlled dolomites under a volcanic activity background.

Keywords: hydrothermal; dolomite; central Sichuan Basin; Middle Permian; ELIP

check for updates

Citation: Gao, J.; Zheng, H.; Liu, B.; Pan, L.; Li, R.; Wu, J.; Yang, X.; Tang, H.; Dong, Y. Genetic Mechanism of Structurally Controlled Dolomites Derived from Seawater-Hydrothermal Mixed Fluids—A Case Study from Middle Permian, Central Sichuan Basin, South China. *Minerals* **2023**, *13*, 758. https://doi.org/10.3390/min13060758

Academic Editor: Luca Aldega

Received: 25 April 2023
Revised: 27 May 2023
Accepted: 28 May 2023
Published: 31 May 2023

Copyright: © 2023 by the authors. Licensee MDPI, Basel, Switzerland. This article is an open access article distributed under the terms and conditions of the Creative Commons Attribution (CC BY) license (https://creativecommons.org/licenses/by/4.0/).

1. Introduction

Hydrothermal dolomitization, which is controlled by basement faults, is widely discussed as a distinctive type of dolomitization on a global scale [1–4]. Generally, this type of dolomitization typically occurs in extensional tectonic geological environments and can result in the formation of exceptional dolomite oil and gas reservoirs [5–7]. Deep hydrothermal fluids, which are associated with tectonic or volcanic activity, are widely recognized as playing a pivotal role in the process of hydrothermal dolomitization, as evidenced by numerous studies in locations such as the Western Canada sedimentary basin, Sichuan Basin, and the Tarim Basin in China [3,8–11]. However, emerging research suggests that seawater also exerts a significant influence on the hydrothermal dolomitization process, potentially serving as the primary source of Mg^{2+} [7,12,13]. The accurate identification of dolomitizing fluids carries important implications for comprehending the mechanisms of dolomitization and predicting the distribution patterns of dolomite reservoirs.

The dolomite layers within the Middle Permian strata of the Sichuan Basin have been repeatedly reported as excellent hydrocarbon reservoirs [12,14–19]. In the central Sichuan Basin, the distribution of Middle Permian dolomite, to some extent, exhibits characteristics that are controlled by basement faults [12,15,20]. Accordingly, most studies suggest that the genesis of the dolomite is associated with deep hydrothermal activity [18–21]. Additionally, the magmatic activity of the Emeishan Large Igneous Province (ELIP) is believed to have created anomalous hydrothermal fluids and the associated thermal effects across the basin [22–24]. However, some studies suggested that the formation processes of Middle Permian dolomites were extremely complex and were the result of multiple stages of superposition [9,16]. Currently, these researches are not clear enough on tracing the sources of diagenetic fluids for each stage, which hinders the understanding of dolomite formation mechanisms. The dolomite bodies in the Middle Permian exhibit a certain degree of heterogeneity in the vertical direction, and the lack of discussion on this phenomenon also limits the prediction of its reservoir distribution.

This study focuses on the typical outcrops and drill cores in the central Sichuan Basin. Microscopic petrology was utilized to characterize different lithofacies types of the dolomite and determine the diagenetic sequence. Geochemical analyses, including C, O, and Sr isotopes and trace elements, were conducted to analyze the geochemical properties of the diagenetic fluids. Subsequently, fluid inclusion analysis was performed to constrain the temperature and salinity of the diagenetic fluids. Our study has effectively revealed the origins of the various stages of dolomitizing fluids in the central Sichuan Basin. We have also discussed the hydrological cycle and water-rock interaction processes, which have explained the spatiotemporal distribution of different types of dolomites. The findings of this study are significant for understanding the formation mechanisms of shallow-buried dolomites affected by igneous activity and have potential implications for the prediction of related dolomite reservoirs.

2. Geological Setting

The Sichuan Basin, located in southwestern China (Figure 1a), is a large hydrocarbon-bearing basin. It is a secondary tectonic unit on the western margin of the Yangtze Platform and has a rhombus-like shape, bordered by several major tectonic belts [25,26]. The Middle Permian strata in the study area comprise the Liangshan Formation (P_2l), Qixia Formation (P_2q), and Maokou Formation (P_2m), in ascending order. The Liangshan Formation was deposited in a coastal environment consisting mainly of coal-bearing mudstone, carbonaceous shale, and sandstone. The Qixia and Maokou Formations were deposited in a stable tropical to subtropical carbonate platform environment, consisting of thick and homogeneous carbonate deposits. The Qixia Formation comprises two members (Qi1 and Qi2), which were deposited in relatively shallower water than the Maokou Formation, particularly in the central Sichuan region, where bioclastic and intraclastic shoals were well developed. The Maokou Formation consists of four members (Mao1 to Mao4). During the early depositional stage of the Maokou Formation, a large-scale transgression occurred in

the study area, leading to a relatively deep-water sedimentary environment throughout the area, with the Mao1 dominated by rhythmic layers of argillaceous limestone and marl. This was followed by a sustained slow regression, with gradually shallowing water depth, and the Mao2 and Mao3 were mainly composed of bioclastic limestone and grainstone. Due to the Dongwu Movement-induced uplift, the top of the Maokou Formation in the study area was extensively eroded [27–29]. The development of dolomite in both vertical and horizontal directions shows strong heterogeneity in the central Sichuan Basin. In the west of the study area (MX42, MX108, GC2, GT2), dolomite mainly develops in Qi2, while in the southeast of the study area (Tl6, XYD, GZS, HLC), dolomite mainly develops in Mao3 and shows the characteristics of distribution along basement faults (Figure 1b) [15,19].

The Sichuan Basin is intersected by NW–SE and NE–SW-oriented basement faults (Figure 1b) [25,30]. These faults, which are confirmed to have been in an extensional state during the mid-to-late Permian, display features of cutting through the Middle Permian strata on seismic profiles [31,32]. The uplift and intense eruption of the ELIP is considered to have caused the tectonic extension background of the mid-late Permian, along with triggering a pronounced anomalous heat effect, manifested by a sustained increase in paleo-heat flow values [22,24]. This anomaly is regional in scale and is not limited to the vicinity of the eruption center. In addition, the abundant ELIP basalts found in drill cores and outcrops in the central Sichuan Basin suggest the occurrence of fault-related hydrothermal activity and anomalous heat effects in this area [33].

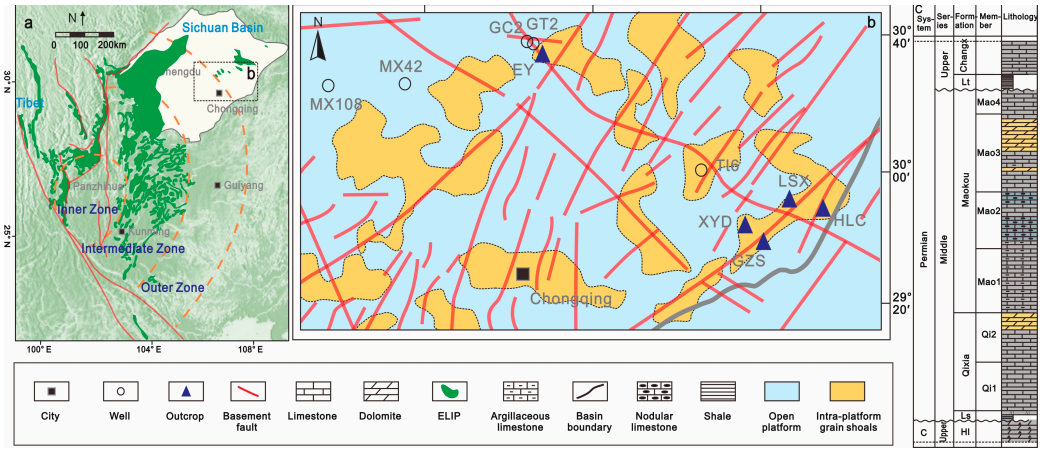


Figure 1. (**a**) The distribution map of ELIP basalts and the location of the Sichuan Basin [33]. (**b**) The location of study outcrops, wells, and the deep basement faults [30]. (**c**) Stratigraphic column of the Middle Permian Formation in the central Sichuan Basin.

3. Materials and Methods

Samples of limestones and dolomites were collected from 7 drill cores and 5 outcrops in the Middle Permian in the central Sichuan Basin (Figure 1b). After detailed observations of outcrops and drill core samples, microscopic petrographic analysis was conducted at the Department of Geological Engineering, Chongqing Jiaotong University, using a polarizing microscope (NIKON LV100N). All thin sections were stained with Alizarin Red to distinguish dolomite from calcite [34]. Subsequently, 1 cm^3 blocks of the samples were cut and observed under a scanning electron microscope (SEM) using an FEI-QUANTA650FEG at the School of Earth and Space Sciences at Peking University. Moreover, energy-dispersive spectroscopy was employed to identify minerals within the carbonate rocks.

Geochemical analyses were conducted at the Key Laboratory of Orogenic Belts and Crustal Evolution and the School of Archaeology and Museology at Peking University. Mineral powders were obtained from the rocks using a micro-drilling technique, with efforts made to minimize potential interferences and contamination among different minerals. For trace element analyses, including rare earth elements (REEs), 80 mg of each sample powder

was dissolved in 1 mL of HNO_3 (1 + 1) and evaporated. The residue was re-dissolved in 1.42 g/mL of HNO_3 and heated for 3 h and then was diluted with ultrapure water and tested for trace element compositions using an inductively coupled plasma mass spectrometer (ICP-MS). The post-Archean average shale (PAAS) was employed to standardize rare earth element concentrations [35]. The $^{87}Sr/^{86}Sr$ ratios were analyzed using a TRITON mass spectrometer. In the pre-treatment stage, 150 mg of sample powder was dissolved in an HCl solution (2.5 mol/L) and centrifuged for 8 min. The clear liquid in the upper layer of the centrifuged tube was then added to a cation exchange column and leached with HCl to extract pure Sr. The NBS987 standard was used to calibrate the obtained $^{87}Sr/^{86}Sr$ ratios, with an average testing precision of $\pm 1.0 \times 10^{-5}$ (2δ). The carbon and oxygen isotope analyses were conducted using the IsoPrime 100 instrument. To prepare the samples for analysis, 200 mg of powder was dissolved in 99% H_3PO_4. The carbon and oxygen isotope values were calibrated against the IAEA CO-8 calcite standard (VPDB). The precision of the analysis was ±0.1‰. The fluid inclusion analysis was carried out at the School of Earth Sciences, Yunnan University. The homogenization temperature (T_h) and final melting temperature ($T_{m\text{-}ice}$) were determined by microthermometry of 100 μm thick, double-sided polished thin sections using a Linkam THMGS600. A cyclic heating method was applied to measure Tm-ice to achieve higher accuracy. Eighty-three fluid inclusions were analyzed in this study, and the salinity was calculated using the calculation formula established by Steele-MacInnis [36,37].

4. Results

4.1. Petrography

4.1.1. Macroscopic Petrology

The macroscopic characteristics of the Middle Permian dolomite in the central Sichuan Basin were examined through observations from field outcrops (Figure 2a–d), rock sections (Figure 2e,f), and core samples (Figure 2a–i), with the typical occurrence of brecciated structures, pore-filling cement minerals, and zebra textures (Figure 2a,b,d). Reticular fractures and dissolved cavities are observed in the matrix replacement dolomite (Rd), which are filled with saddle dolomite cement (Sd) (Figure 2a,b). Bed-parallel fractures filled with Sd are also discovered in the outcrop (Figure 2c). The calcite cement (Cc), quartz cement (Qz), and Sd fill the pores successively in the dissolved cavities (Figure 2d), which is more clearly observed in the thin rock sections and core samples (Figure 2e,g). The zebra texture is composed of alternating layers of matrix dolomite and Sd (Figure 2f). Correspondingly, the dissolution pores and network cracks, which are partially filled with Sd and bitumen (Bit), are also observed in the cores (Figure 2h,i).

4.1.2. Microscopic Petrography

The Middle Permian dolomites are composed of three types of matrix-replaced dolomites (Rd1, Rd2, and Rd3) and dolomite cement (Sd) in the central Sichuan Basin. Rd1, which develops in an incompletely dolomitized state within the host limestone (Figure 3), is present in low abundance (<10%) in the dolomite formation and is composed of fine-grained dolomite particles with planar crystals (Figure 3). Dolomitization preferentially occurred around stylolite and within the mudstone matrix in the host limestone, leading to the formation of Rd1 (Figure 3a,b). Rd1 displays rhombic shapes with fog center-bright edge structure (Figure 3c,d). Under cathodoluminescence (CL), Rd1 displays a dark red luminescence, while the host limestone shows almost no luminescence (Figure 3e,f).

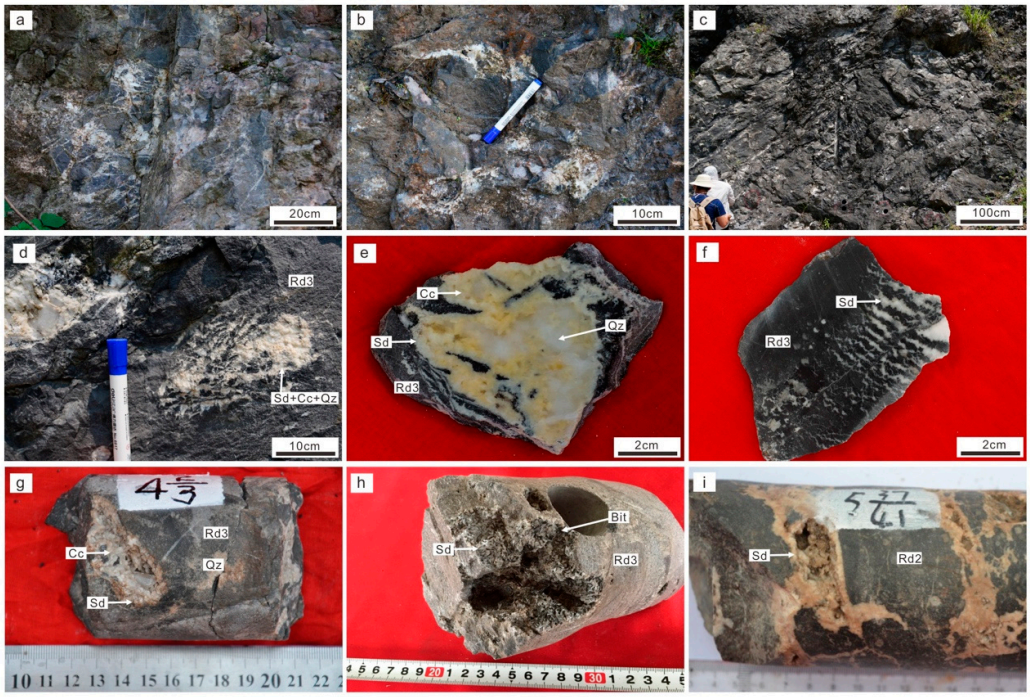


Figure 2. Field outcrop, core, and rock slice photographs of Middle Permian dolomite, central Sichuan Basin. (**a**) Breccia structures, GZS, P_2m^3; (**b**) Calcite and dolomite cement filling in cracks and dissolution holes, GZS, P_2m^3; (**c**) Stratiform fractures developed with calcite and dolomite cement filling, HLC, P_2m^3; (**d**) Dissolution holes filled with Sd, Cc, and Qz, HLC, P_2m^3; (**e**) Sd, Cc, and Qz filling successively from the surrounding rocks to the center of the holes, GZS, P_2m^3; (**f**) The crack filled with Sd and the Rd3 surrounding rock formed a zebra structure, XYD, P_2m^3; (**g**) Sd filling in the edge of the dissolution hole, Cc filling in the center, TL6, P_2m^3; (**h**) Sd and Bit filling in the pores, MX42, P_2q^2; (**i**) Rd2 surrounding rock with incompletely filled crystal cavity of Sd, TL7, P_2m^3.

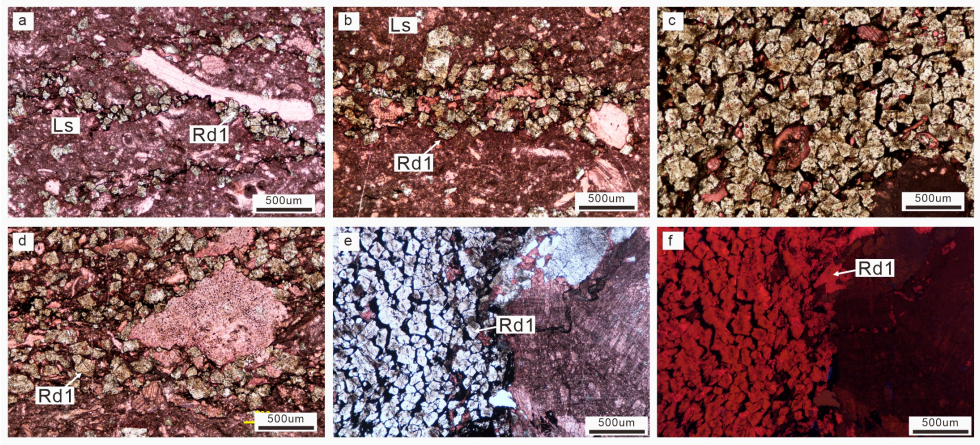


Figure 3. The photomicrograph and cathodoluminescence photo of Rd1. (**a**,**b**) Rd1 occurs around the stylolites, and the mudstone matrix surrounding the bright grains undergoes preferential dolomitization, EY, P_2m^3; (**c**). The Rd1 crystals are rhombic and have a foggy center-bright edge structure, EY, P_2m^3; (**d**) Rd1 is formed by preferential dolomitization of the mudstone matrix surrounding the bright grains, EY, P_2m^3; (**e**). Rd1 and Bit filling in the fractures, XYD, P_2m^3; (**f**) The cathodoluminescence image of (**e**) shows that Rd1 emits dark red light while the limestone barely luminesces.

The content of Rd2 in the dolostone unit is approximately 40%–50%, consisting of fine to medium-sized dolomite crystals (50~250 μm) with planar crystals (Figure 4). The dolomite crystals in Rd2 generally lack the original limestone textures, showing interlocking mosaic contacts with bright rimmed edges (Figure 4a). Rd2 displays the development of a reticulated crack system and brighter red luminescence than Rd1 under cathodoluminescence (CL), while the cement in the crack system emits similar bright red luminescence (Figure 4b,c). Cracks filled with both calcite and quartz are developed in Rd2 (Figure 4d). Cracks filled with Sd, which cuts across Rd2, display a relatively bright orange-red luminescence in both minerals under CL (Figure 4e,f).

Rd3 constitutes 30%–40% of the volume of the dolomite, consisting of medium- to coarse-sized (250 μm–2 mm) crystals with curved surfaces (Figure 5a). Saddle dolomite (Sd) accounts for approximately 10%–20% of the volume of the dolomite and fills the fractures and pores of the matrix-replaced dolomite as cement (Figure 5b). Typically, some Sd exhibit large crystals, which can exceed 2 mm in size, and display strong undulatory extinction under cross-polarized light (Figure 5e). Rd3 and Sd display intense orange-red luminescence under CL, while the quartz (Qz) and calcite (Cc) types of cement filling the pores are relatively dim (Figure 5c–f). Rd2, Rd3, and Sd are closely developed from the host rock to the pores, with Rd2 and Rd3 exhibiting relatively dim orange-red light under CL, while Sd displays a strong red halo. A large number of hydrothermal minerals, including pyrite, siderite, and fluorite, filled in the pores of Rd3 and Sd (Figure 6d–f).

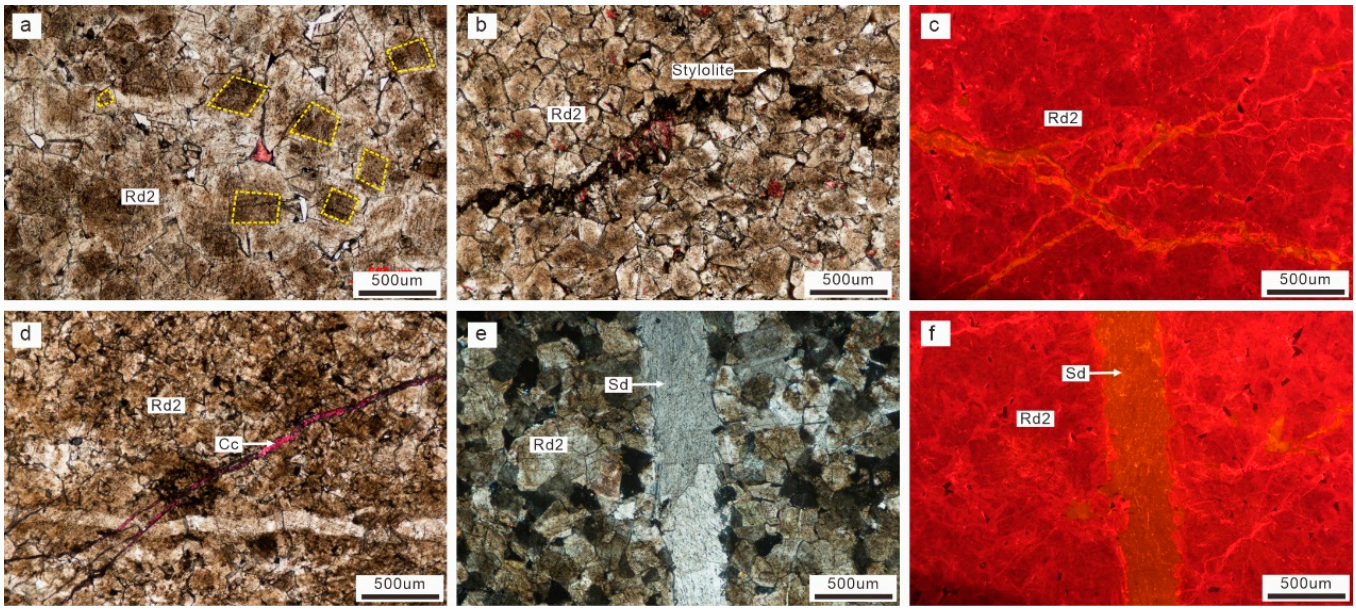


Figure 4. The photomicrograph and cathodoluminescence photo of Rd2. (**a**) The Rd2 crystals exhibit an interlocking contact morphology with a turbid Rd1 core and a bright halo at the edge, EY, P_2m^3; (**b**) Rd2 is cut by stylolite, GDS, P_2m^3; (**c**) The cathodoluminescence image shows that Rd2 emits a darker red light (but brighter than Rd1), while the network of cracks emits a brighter red light, GDS, P_2m^3; (**d**) Rd2 crystals are cut by cracks filled with calcite and dolomite, HLC, P_2m^3; (**e**) Cracks filled with Sd in the Rd2 dolomites, observed under crossed polarized light, GDS, P_2m^3; (**f**) The cathodoluminescence image of e shows that both Rd2 and Sd within the cracks emit a bright orange-red light.

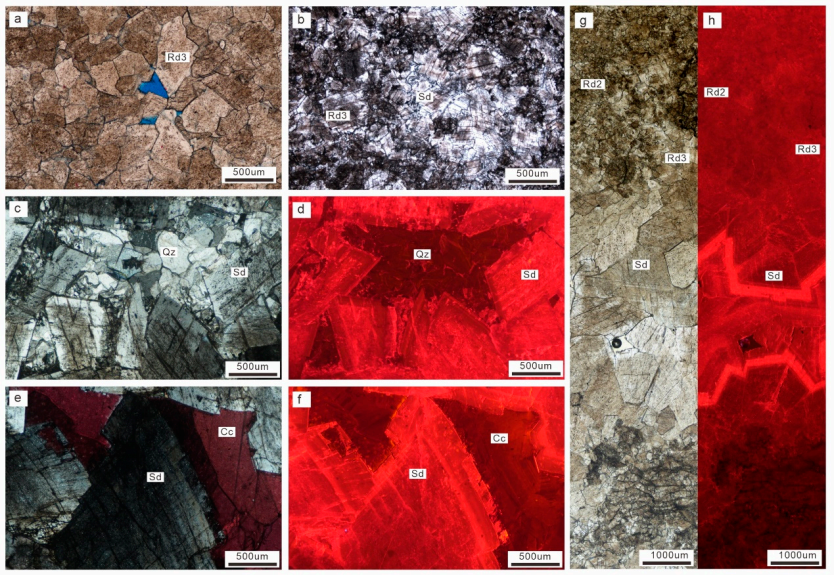


Figure 5. The photomicrograph and cathodoluminescence photo of Rd3 and Sd. (**a**) Rd3 crystals exhibit an interlocking texture with intercrystalline pores (blue phase), EY, P_2m^3; (**b**) Sd-filled pores are developed within the Rd3 crystals, GT2, P_2q^2; (**c**) The cross-polarized light photograph reveals the presence of Sd and Qz filling the cavities within Rd3 crystals, GZS, P_2m^3; (**d**) The cathodoluminescence photograph of (**c**) shows that Sd emits brighter orange-red light than Qz, which emits dimmer light; (**e**) The cross-polarized light photograph of Sd and Cc reveals strong wave extinction of Sd, GZS, P_2m^3; (**f**) The cathodoluminescence photograph of (**e**) shows Sd emitting intense orange-red light, while Cc emits relatively dimmer orange-red light; (**g**) Rd2, Rd3, and Sd are sequentially filled from the host rock to the fracture, XYD, P_2m^3; (**h**) The cathodoluminescence photograph of (**g**) shows that Rd2 and Rd3 crystals emit dim red light, while Sd exhibits an interlocking texture emitting bright red light at the rim.

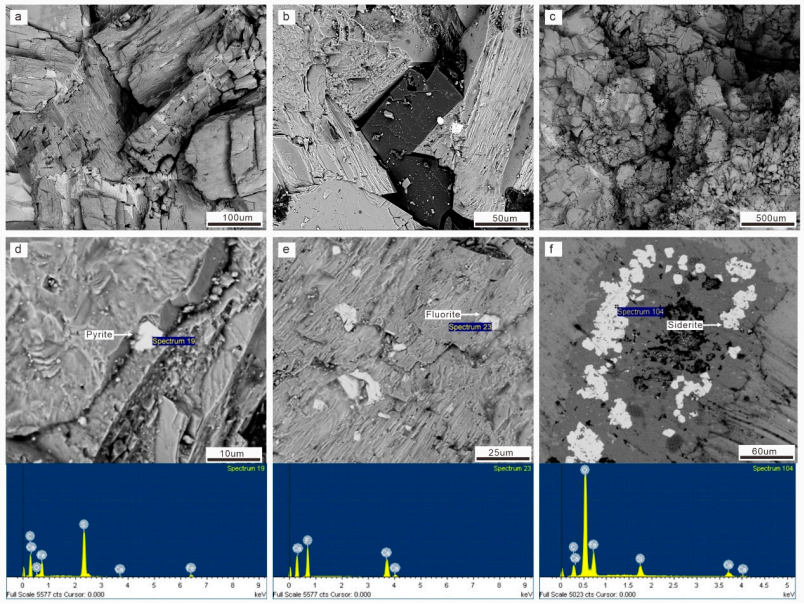


Figure 6. The scanning electron microscope images and energy spectra of dolomite minerals. (**a**) The intercrystalline pores are well-developed in Rd3, EY, P_2m^3; (**b**) Bitumen fill the pores of Rd3, GT2, P_2q^2; (**c**) The edges of the crystal cavity in Rd3 exhibit a fractured state, EY, P_2m^3; (**d**) Pyrite is present in Rd3, MX42, P_2q^2; (**e**) Fluorite is observed in Rd3, MX42, P_2q^2; (**f**) Siderite develops in Rd3, EY, P_2m^3.

4.2. Microthermometry and Salinity

Gas-liquid two-phase fluid inclusions in the form of isolated and fluid inclusion assemblage (FIA) were analyzed in Rd2, Rd3, and Sd (Figures 7 and 8, Table 1). In Rd2, T_h values range from 83 to 134 °C (average 109.4 °C), and salinity values calculated using $T_{m\text{-}ice}$ range from 4.3 wt% to 7.3 wt% (average 5.7 wt%). The temperatures and salinities of fluid inclusions (FI) in Rd3 are higher than those in Rd2, ranging from 104 to 200 °C (average 140 °C) and 5.1 wt% to 22.1 wt% (average 15.1 wt%). FIs in Sd feature the highest temperature and salinity values, ranging from 118 to 208 °C (average 160.8 °C) and 8.4 wt% to 20.1 wt% (average 16.1 wt%).

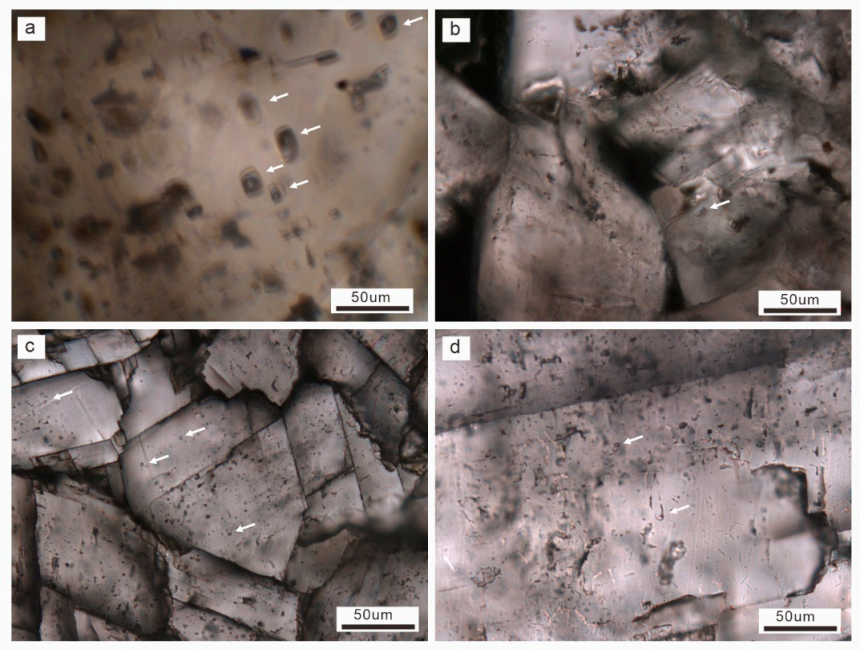


Figure 7. Microphotographs of fluid inclusions in the dolomite. (**a**) Fluid inclusions assemblage (FIA) in Rd3, XYD, P_2m^3; (**b**) Isolated fluid inclusions in Rd3, GZS, P_2m^3; (**c**) Isolated fluid inclusions in the minerals of Rd2, MX42, P_2q^2; (**d**) Isolated fluid inclusions in Sd, HLC, P_2m^3.

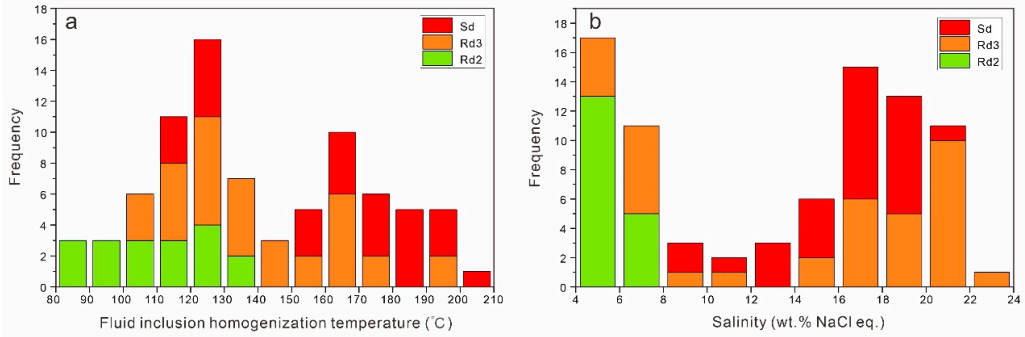


Figure 8. Histogram of temperature and salinity of gas-liquid two-phase fluid inclusions in Middle Permian dolomite in central Sichuan Basin. (**a**) Histogram of homogenization temperature frequency of fluid inclusions (**b**) Histogram of salinity frequency of fluid inclusions.

Table 1. Data of Fluid inclusions in the Middle Permian dolomite in the central Sichuan Basin.

Sample	Mineral Type	Occurrences	Size (μm)	V%	Th (°C)	Tm (°C)	Salinity (wt% NaCl eq.)
GT2-11	Rd2	Isolated	4	5	98	−2.6	4.3
GT2-11	Rd2	Isolated	3	5	83	−4.3	6.9
GT2-11	Rd2	Isolated	3	5	102	−3.2	5.3
GT2-11	Rd2	Isolated	5	5	86	−3.3	5.4
GT2-11	Rd2	Isolated	2	5	94	−3.5	5.7
GT2-13	Rd2	Isolated	4	5	113	−4.1	6.6
GT2-13	Rd2	Isolated	4	5	132	−2.9	4.8
GT2-13	Rd2	Isolated	4	5	121	−3.4	5.6
GT2-13	Rd2	Isolated	5	10	108	−3.7	6.0
GT2-13	Rd2	Isolated	5	5	115	−3	5.0
GT2-10	Rd2	Isolated	4	5	125	−3.3	5.4
GT2-10	Rd2	Isolated	5	5	107	−3.5	5.7
GT2-10	Rd2	Isolated	3	5	116	−4.5	7.2
GT2-10	Rd2	Isolated	4	5	128	−4.6	7.3
GC2-3	Rd2	Isolated	3	5	95.00	−3.1	5.1
GC2-3	Rd2	Isolated	4	5	86.00	−3.5	5.7
GC2-3	Rd2	Isolated	4	5	127.00	−2.9	4.8
GC2-3	Rd2	Isolated	3	5	134.00	−3.2	5.3
GC2-3	Rd3	Isolated	5	10	197.00	−17.6	20.7
GC2-3	Rd3	Isolated	5	10	199.00	−16.9	20.1
GC2-10	Rd3	Isolated	6	10	160.00	−18.3	21.2
GC2-10	Rd3	Isolated	4	20	162.00	−16.2	19.6
GC2-10	Rd3	Isolated	4	10	170.00	−18.6	21.4
GC2-10	Rd3	Isolated	4	5	147.00	−17.3	20.4
GC2-10	Rd3	Isolated	4	5	170.00	−15.2	18.8
GC2-6	Rd3	Isolated	4	5	168.00	−14.1	17.9
GC2-6	Rd3	Isolated	5	10	169.00	−15.8	19.3
GC2-6	Rd3	Isolated	5	10	166.00	−19.6	22.1
GC2-6	Rd3	Isolated	4	5	159.00	−18.7	21.5
GC2-6	Rd3	Isolated	4	5	166.00	−14.2	18.0
GC2-6	Rd3	Isolated	4	5	153.00	−13.3	17.2
MX42-4	Rd3	Isolated	6	5	148.00	−12.9	16.8
MX42-4	Rd3	Isolated	4	5	128.00	−10.7	14.7
MX42-4	Rd3	Isolated	4	5	135.00	−11.4	15.4
MX42-4	Rd3	Isolated	5	5	121.00	−12.3	16.2
MX42-4	Rd3	Isolated	4	5	104.00	−3.1	5.1
MX42-4	Rd3	Isolated	4	5	106.00	−4.2	6.7
MX42-4	Rd3	Isolated	3	5	126.00	−5.9	9.1
MX42-6	Rd3	Isolated	3	5	118.00	−4.3	6.9
MX42-6	Rd3	Isolated	4	5	119.00	−3.7	6.0
MX42-6	Rd3	Isolated	4	5	121.00	−4.2	6.7
MX42-6	Rd3	Isolated	5	5	123.00	−4.4	7.0
MX42-6	Rd3	Isolated	4	5	123.00	−3.2	5.3
TL6-14	Rd3	Isolated	4	5	127.60	−7.7	11.3
TL6-14	Rd3	Isolated	5	5	132.30	−18.2	21.1
TL6-14	Rd3	Isolated	5	10	134.50	−18.8	21.5
TL6-14	Rd3	Isolated	5	10	141.60	−19.3	21.9
TL6-14	Rd3	Isolated	5	5	132.70	−17.4	20.5
TL6-20	Rd3	Isolated	5	5	105.30	−4.6	7.3
TL6-20	Rd3	Isolated	3	10	113.20	−3.2	5.3
TL6-20	Rd3	Isolated	3	5	111.30	−3.5	5.7
TL6-20	Rd3	Isolated	4	5	112.90	−13.2	17.1
TL6-20	Rd3	Isolated	4	5	139.6	−16.4	19.8
TL6-20	Rd3	Isolated	4	5	132.1	−15.7	19.2
GC2-3	Sd	Cluster	6	5	185	−16.8	20.1
GC2-3	Sd	Cluster	6	5	182	−15.3	18.9
GC2-3	Sd	Cluster	5	10	178	−14.7	18.4
GC2-3	Sd	Cluster	4	5	187	−15.9	19.4
GC2-3	Sd	Cluster	4	5	191	−15.5	19.0

Table 1. *Cont.*

Sample	Mineral Type	Occurrences	Size (μm)	V%	Th (°C)	Tm (°C)	Salinity (wt% NaCl eq.)
GC2-6	Sd	Cluster	4	10	162	−13.2	17.1
GC2-6	Sd	Cluster	3	5	157	−12.4	16.3
GC2-6	Sd	Cluster	5	10	168	−14.7	18.4
GC2–6	Sd	Cluster	4	5	174	−14.1	17.9
GC2-6	Sd	Cluster	6	5	208	−14.8	18.5
TL6-17	Sd	Cluster	5	10	157	−8.8	12.6
TL6-17	Sd	Cluster	6	10	191	−11.6	15.6
TL6-17	Sd	Cluster	4	10	187	−13.5	17.3
TL6-17	Sd	Cluster	4	5	196	−14.2	18.0
TL6-17	Sd	Cluster	4	5	183	−12.3	16.2
TL6-17	Sd	Cluster	5	10	164	−14.5	18.2
TL6-22	Sd	Cluster	4	10	121.4	−5.4	8.4
TL6-22	Sd	Cluster	3	10	117.6	−14.1	17.9
TL6-22	Sd	Cluster	7	5	119.3	−6.2	9.5
TL6-22	Sd	Cluster	4	5	117.6	−8.3	12.0
TL6-22	Sd	Cluster	4	10	120.4	−13.4	17.3
TL6-22	Sd	Cluster	3	5	177.4	−12.5	16.4
TL6-22	Sd	Cluster	3	10	162.2	−10.9	14.9
TL6-22	Sd	Cluster	4	10	174.3	−14.4	18.1
TL6-22	Sd	Cluster	4	10	157.3	−11.7	15.7
MX42-6	Sd	Isolated	4	5	124	−9.3	13.2
MX42-6	Sd	Isolated	4	5	121	−7.8	11.5
MX42-6	Sd	Isolated	4	5	120	−11.2	15.2

4.3. Carbon, Oxygen, and Strontium Isotopes

Generally, limestone, Rd1, Rd2, Rd3, and Sd all exhibit similar $\delta^{13}C$ values, with ranges of 1.63 to 5.15‰ (average 3.47‰), 2.73 to 3.05‰ (average 2.93‰), 3.06 to 4.46‰ (average 3.87‰), −0.7 to 6.14‰ (average 3.93‰), and 2.93 to 5.0‰ (average 3.77‰), respectively. For oxygen isotopes, Rd1 has the highest $\delta^{18}O$ values among all the dolomites, ranging from −5.73 to −3.63‰ (average −4.59‰), and is close to the $\delta^{18}O$ values of limestone with a range from −7.32 to −2.92‰ (average −5.92‰). The $\delta^{18}O$ values of Rd2 are slightly lower than those of Rd1, ranging from −7.68 to −6.21‰ (average −6.85‰). The $\delta^{18}O$ values of Rd3 and Sd are the most negative among all the dolomites, with ranges of −9.45 to −6.80‰ (average −8.24‰) and −8.4 to −6.99‰ (average −7.95‰) (Figure 10, Table 2).

Table 2. Carbon, oxygen, and strontium isotopes in the Middle Permian dolomite in the central Sichuan Basin.

Sample	Mineral Type	$\delta^{13}C$	$\delta^{18}O$	$^{87}Sr/^{86}Sr$	Error
MX108–1	Limestone	3.59	−7.32		
MX42–1	Limestone	3.67	−7.62		
EY–1	Limestone	2.94	−4.8	0.707219	0.000018
EY–2	Limestone	4.49	−4.15		
EY–3	Limestone	4.97	−3.97		
EY–4	Limestone	5.15	−4.42	0.707523	0.000016
EY–5	Limestone	3.77	−4.56		
EY–6	Limestone	4.25	−6.95		
LSX–1	Limestone	3.92	−5.55		
LSX–2	Limestone	4.40	−6.50		
HLC–1	Limestone	2.30	−7.20	0.7072	0.000017
HLC–2	Limestone			0.7074	0.000019
HLC–3	Limestone			0.7077	0.000020
HLC–4	Limestone			0.7080	0.000021
HLC–5	Limestone			0.7076	0.000016
HLC–6	Limestone			0.7076	0.000017

Table 2. *Cont.*

Sample	Mineral Type	$\delta^{13}C$	$\delta^{18}O$	$^{87}Sr/^{86}Sr$	Error
HLC–7	Limestone			0.7070	0.000023
GC2–1	Limestone	1.63	−2.92	0.707512	0.000022
GC2–2	Limestone	2.32	−3.59	0.7070536	0.000019
GT2–1	Limestone	2.43	−6.7		
GT2–2	Limestone	2.84	−6.36		
GT2–3	Limestone	2.63	−6.01		
GT2–4	Limestone	3.26	−7.14		
TL6–2	Limestone	3.23	−7.76	0.707933	0.000017
TL6–3	Limestone	3.47	−6.71	0.707965	0.000019
TL6–4	Limestone	3.98	−7.35	0.707829	0.000020
TL6–5	Limestone			0.707774	0.000021
TL6–6	Limestone			0.707028	0.000023
TL6–7	Limestone			0.708009	0.000019
TL6–8	Limestone	3.64	−6.44	0.707112	0.000016
GT2–5	Rd1	2.73	−3.63	0.707165	0.000018
GT2–6	Rd1	3.05	−4.05	0.706572	0.000017
GT2–7	Rd1	3.04	−5.73	0.707091	0.000021
GT2–8	Rd1	3.03	−4.26	0.705214	0.000022
GT2–9	Rd1	2.82	−5.26	0.705723	0.000023
EY–7	Rd2	4.46	−6.21	0.706548	0.000017
EY–8	Rd2	4.1	−6.4	0.708002	0.000021
EY–9	Rd2	3.83	−6.76	0.707566	0.000014
GT2–10	Rd2	3.06	−6.81		
GT2–11	Rd2	4.22	−6.83	0.707457	0.000025
EY–10	Rd2	3.56	−6.83		
GT2–12	Rd2	4.17	−6.87	0.708328	0.000023
EY–11	Rd2	3.8	−7.17	0.707719	0.000016
GT2–13	Rd2	3.91	−7.68		
EY–12	Rd2	3.64	−6.94	0.7074	0.000023
HLC–8	RD3	3.40	−7.90	0.7086	0.000013
HLC–9	RD3	1.80	−6.80		
HLC–7	RD3	−0.70	−7.70		
GC2–3	RD3	3.44	−7.64		
GC2–4	RD3	3.74	−7.77	0.709194	0.000017
MX108–2	RD3	4.63	−7.96		
MX42–2	RD3	5.00	−7.99	0.707457	0.000016
MX42–3	RD3	4.86	−8.09		
MX42–4	RD3	5.28	−8.12		
MX108–3	RD3	4.34	−8.13	0.708571	0.000021
MX42–5	RD3	4.44	−8.19		
MX108–5	RD3	5.36	−8.22		
M11–1	RD3	6.14	−8.45		
WJ1–1	RD3	5.46	−8.49		
MX42–6	RD3	5.00	−9.02		
GT2–12	RD3	3.49	−9.45		
TL6–10	RD3	2.57	−7.96		
TL6–11	RD3	4.50	−8.30		
TL6–12	RD3	3.90	−8.40		
TL6–13	RD3	3.60	−7.90		
TL6–14	RD3	4.30	−8.30	0.709234	0.000022
TL6–15	RD3	2.80	−8.40	0.708309	0.000013
TL6–16	RD3	3.10	−8.80	0.709088	0.000021
TL6–17	SD			0.708508	0.000015
TL6–18	SD			0.708399	0.000016
TL6–19	RD3	5.00	−7.90	0.708418	0.000013
TL6–20	RD3	4.70	−8.10	0.708201	0.000017
EY–13	RD3	4.10	−8.30	0.708234	0.000018
EY–14	RD3	4.20	−8.21	0.708332	0.000020
GC2–5	SD	3.25	−7.83	0.709286	0.000021

Table 2. *Cont.*

Sample	Mineral Type	$\delta^{13}C$	$\delta^{18}O$	$^{87}Sr/^{86}Sr$	Error
GC2–6	SD	3.78	−7.95	0.709453	0.000016
GC2–8	SD	3.37	−8.27		
GC2–9	SD	3.06	−7.37		
TL6–21	SD	2.93	−8.00	0.708655	0.000017
TL6–22	SD	3.44	−7.94	0.708009	0.000018
TL6–23	SD	3.53	−6.99	0.708508	0.000019
TL6–24	SD	3.48	−8.16	0.708399	0.000012
TL6–25	SD	2.95	−7.86		
HLC–10	SD			0.708571	0.000018
HLC–11	SD			0.70782	0.000013
HLC–12	SD			0.707728	0.000015
HLC–13	SD			0.707457	0.000014
HLC–14	SD	3.10	−8.40	0.708462	0.000021
GZS–1	RD3	3.10	−8.80	0.708653	0.000021
GZS–2	RD3	2.90	−8.60	0.708752	0.000022
GZS–3	RD3	2.90	−8.50	0.708321	0.000013
GZS–4	RD3	2.80	−8.40	0.709026	0.000017
GZS–5	RD3	3.90	−8.40	0.708908	0.000014
GZS–7	RD3	4.00	−8.40	0.707982	0.000019
GZS–9	RD3	4.20	−8.30	0.708132	0.000015
GZS–10	RD3	4.30	−8.30	0.708293	0.000017
GZS–11	RD3	4.50	−8.30	0.708398	0.000026
GZS–12	RD3	4.50	−8.30	0.709031	0.000009
GZS–13	SD	4.60	−8.20	0.708432	0.000012
GZS–14	SD	4.60	−8.20	0.70889	0.000016
GZS–15	SD	4.40	−8.10	0.708768	0.000016
GZS–16	SD	4.50	−8.10	0.708807	0.000023
GZS–17	SD	4.70	−8.10	0.708219	0.000021
GZS–18	SD	3.60	−7.90	0.707893	0.000019
GZS–19	SD	5.00	−7.90	0.708675	0.000012
GZS–20	SD	3.50	−7.80	0.708065	0.000011

4.4. Trace and Rare Earth Elements

The REE patterns of limestone and Rd2 are relatively flat with slight LREE depletion, i.e., the lowest LREE/HREE ratios of 0.66 and 0.50, respectively (Figure 9a,b, Table 3). Rd3 and Sd exhibit average LREE/HREE ratios of 1.17 and 1.97, respectively, showing slight LREE enrichment (Figure 9c,d, Table 3). Notably, the presence of significant Ce anomalies was not observed in all of the examined samples (Figure 10a). In Rd3 and Sd samples, the Eu contents exhibit prominent positive anomalies on the REE patterns (Figure 9c,d). The average Eu/Eu* values of Rd3 and Sd are 6.6 and 11.7 (Figure 11b–d). Limestone shows the highest Sr content (average 724 ppm) and the lowest Mn content (average 64.5 ppm) (Figure 11c, Table 3). The average Sr and Mn contents of Rd2 are 197.1 ppm and 165 ppm (Figure 11c, Table 3). The Sr contents of Rd3 and Sd are 131.3 ppm and 228.4 ppm, and the Mn contents are 139.7 ppm and 170.3 ppm (Figure 11c, Table 3).

The $^{87}Sr/^{86}Sr$ ratios of limestone and Rd1 are the lowest among all the samples, ranging from 0.707219 to 0.708009 (average 0.707526) and 0.706914 to 0.707723 (average 0.707293), falling within the distribution range of the Permian seawater (0.7068–0.7081) [38,39]. The $^{87}Sr/^{86}Sr$ ratios of Rd2 are slightly higher than those of Rd1, ranging from 0.7074 to 0.708328 (average 0.70776), with the ratios of a few samples higher than the Permian seawater range. The $^{87}Sr/^{86}Sr$ ratios of Rd3 and Sd samples are the highest among all the samples, ranging from 0.7086 to 0.709234 (average 0.7085) and 0.707457 to 0.709453 (average 0.708426), respectively, in which the ratios most of the samples are higher than the Permian seawater distribution range (Figure 12).

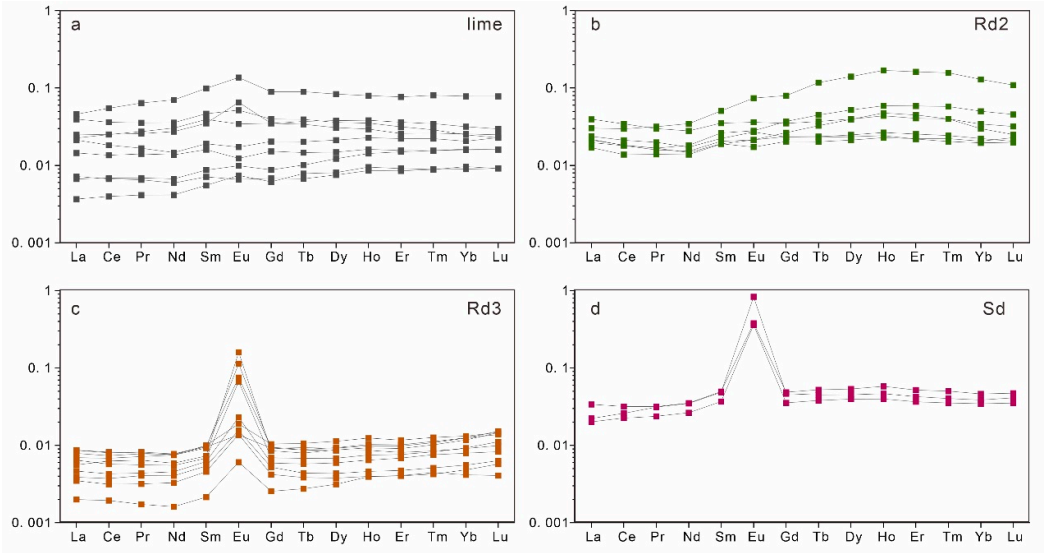


Figure 9. The patterns of PAAS–normalized Rare Earth Elements (REE) in Middle Permian samples from the central Sichuan Basin. (**a**) The patterns of REE for limestone samples; (**b**) The patterns of REE for Rd2 samples; (**c**) The patterns of REE for Rd3 samples; (**d**) The patterns of REE for Sd samples.

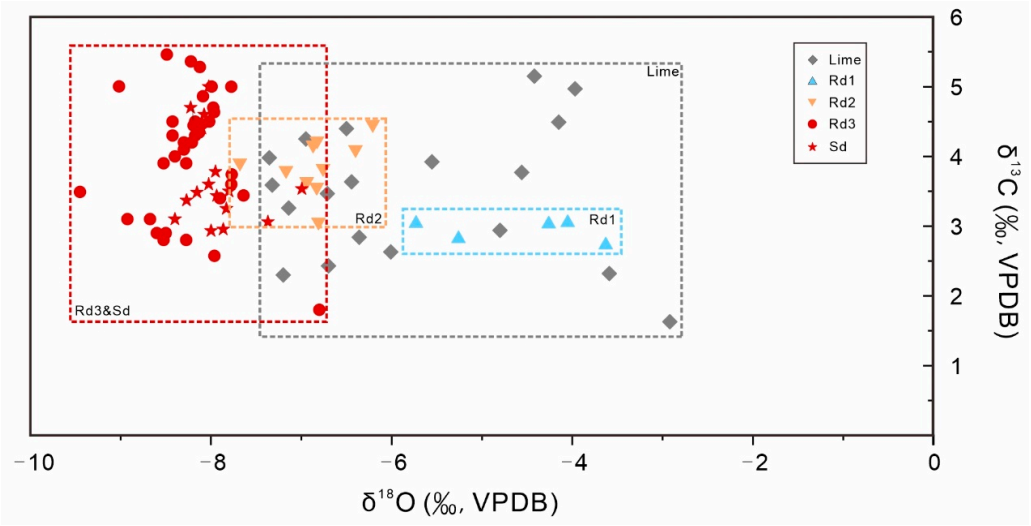


Figure 10. Scatter plots of $\delta^{18}O$ (VPDB) and $\delta^{13}C$ (VPDB) for collected samples in the Middle Permian, middle– to eastern–Sichuan Basin.

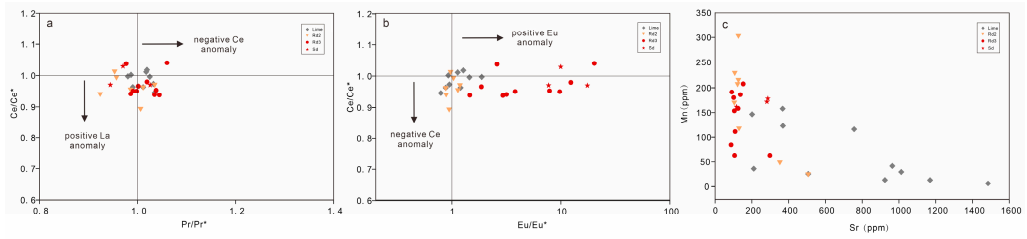


Figure 11. Scatter plots of (**a**) Ce/Ce* versus Pr/Pr*, (**b**) Ce/Ce* versus Eu/Eu*, and (**c**) Sr versus Mn for collected samples in the Middle Permian, central Sichuan Basin.

Table 3. Trace and rare earth elements in the Middle Permian dolomite in the central Sichuan Basin.

Sample	Mineral Type	Mn	Sr	La	Ce	Pr	Nd	Sm	Eu	Gd	Tb	Dy	Ho	Er	Tm	Yb	Lu	Ce/Ce*	Pr/Pr*	Eu/Eu*
MX108–1	Limestone	146.466	201.047																	
MX42–1	Limestone	122.775	369.039																	
EY–1	Limestone	36.244	210.065	1.761	3.194	0.361	1.330	0.321	0.063	0.240	0.035	0.192	0.037	0.097	0.013	0.075	0.010	0.964	0.990	1.201
EY–2	Limestone	6.353	1484.558	0.321	0.589	0.066	0.221	0.049	0.008	0.041	0.006	0.040	0.009	0.026	0.004	0.027	0.004	0.974	1.032	0.947
EY–3	Limestone	29.669	1012.368	0.163	0.350	0.042	0.155	0.038	0.009	0.037	0.007	0.043	0.010	0.028	0.004	0.029	0.004	1.017	1.019	1.272
EY–4	Limestone	13.350	1169.095	0.297	0.605	0.070	0.250	0.060	0.012	0.053	0.009	0.065	0.015	0.046	0.007	0.048	0.007	1.011	1.018	1.130
EY–5	Limestone	25.780	506.701	0.947	1.612	0.169	0.547	0.131	0.021	0.123	0.018	0.113	0.024	0.068	0.010	0.062	0.010	0.964	1.011	0.878
EY–6	Limestone	13.566	923.556	0.646	1.194	0.143	0.511	0.110	0.015	0.092	0.013	0.079	0.017	0.048	0.007	0.049	0.007	0.947	1.035	0.791
TL6–1	Limestone	115.859	756.184	2.046	4.834	0.650	2.622	0.682	0.166	0.541	0.080	0.446	0.084	0.236	0.036	0.236	0.034	0.996	1.025	1.448
TL6–5	Limestone	157.785	367.510	1.009	2.210	0.278	1.135	0.270	0.042	0.211	0.030	0.164	0.031	0.079	0.012	0.077	0.011	1.002	0.987	0.927
TL6–7	Limestone	41.719	963.803	1.105	2.224	0.261	1.020	0.240	0.080	0.211	0.033	0.202	0.040	0.111	0.016	0.095	0.013	0.997	0.980	1.876
EY–7	Rd2	207.785	122.111	0.877	1.589	0.161	0.570	0.141	0.026	0.142	0.021	0.132	0.028	0.078	0.011	0.067	0.009	1.013	0.953	0.973
EY–8	Rd2	49.420	352.488	1.760	3.044	0.303	1.041	0.242	0.044	0.211	0.033	0.211	0.046	0.125	0.018	0.103	0.014	0.995	0.957	1.034
EY–9	Rd2	229.331	107.109	0.757	1.219	0.141	0.515	0.130	0.026	0.160	0.029	0.210	0.050	0.138	0.018	0.090	0.011	0.895	1.006	0.943
EY–10	Rd2	303.567	126.992	1.348	2.613	0.321	1.289	0.349	0.090	0.482	0.105	0.750	0.178	0.500	0.071	0.389	0.048	0.957	0.986	1.136
GT2–12	Rd2	117.987	130.118	1.054	1.867	0.202	0.642	0.154	0.033	0.141	0.021	0.125	0.025	0.067	0.009	0.059	0.009	0.972	1.035	1.186
EY–11	Rd2	170.466	104.428	0.967	1.599	0.170	0.677	0.181	0.034	0.223	0.040	0.278	0.062	0.180	0.026	0.151	0.020	0.942	0.924	0.886
EY–10	Rd2	215.764	126.785																	
EY–12	Rd2	25.780	506.701	0.947	1.612	0.169	0.547	0.131	0.021	0.123	0.018	0.113	0.024	0.068	0.010	0.062	0.010	0.964	1.011	0.878
MX108–2	RD3	186.117	137.456	0.309	0.601	0.073	0.279	0.069	0.023	0.063	0.009	0.060	0.013	0.036	0.006	0.040	0.006	0.967	1.002	1.864
MX42–2	RD3	179.965	101.122	0.155	0.277	0.032	0.123	0.031	0.017	0.025	0.003	0.020	0.004	0.012	0.002	0.014	0.003	0.942	0.986	3.169
MX42–3	RD3	158.206	125.373	0.387	0.721	0.081	0.280	0.064	0.138	0.056	0.008	0.049	0.010	0.030	0.005	0.037	0.007	0.980	1.019	12.347
MX42–4	RD3	153.474	104.804	0.173	0.328	0.041	0.151	0.037	0.019	0.032	0.004	0.023	0.005	0.015	0.002	0.017	0.003	0.938	1.045	2.936
MX108–3	RD3	111.122	108.942	0.250	0.552	0.065	0.219	0.050	0.194	0.051	0.007	0.047	0.010	0.028	0.005	0.035	0.006	1.040	1.060	20.268
MX42–5	RD3	207.578	152.937	0.384	0.707	0.083	0.290	0.067	0.092	0.057	0.008	0.050	0.011	0.031	0.005	0.038	0.006	0.954	1.038	7.858
MX108–5	RD3	61.930	106.087	0.207	0.379	0.045	0.170	0.043	0.028	0.036	0.005	0.032	0.007	0.021	0.003	0.024	0.004	0.951	0.991	3.806
M11–1	RD3	61.995	298.129	0.089	0.171	0.018	0.060	0.015	0.007	0.015	0.002	0.017	0.004	0.013	0.002	0.013	0.002	1.037	0.977	2.591
WJ1–1	RD3	84.911	86.910	0.351	0.649	0.079	0.287	0.066	0.017	0.056	0.008	0.046	0.009	0.025	0.004	0.027	0.004	0.939	1.035	1.459
MX42–6	RD3	191.254	90.783	0.286	0.504	0.057	0.205	0.047	0.081	0.042	0.006	0.036	0.008	0.023	0.004	0.028	0.005	0.951	0.998	9.765
TL6–17	SD	161.454	116.765	1.511	2.809	0.321	1.312	0.342	0.461	0.294	0.047	0.286	0.061	0.160	0.023	0.139	0.021	0.971	0.945	7.716
TL6–18	SD	171.624	281.809	0.994	2.292	0.317	1.301	0.334	1.012	0.281	0.040	0.240	0.049	0.131	0.018	0.117	0.018	0.971	1.026	17.510
TL6–22	SD	177.983	286.753	0.897	1.991	0.241	0.985	0.253	0.438	0.214	0.034	0.211	0.042	0.113	0.016	0.104	0.015	1.029	0.970	9.969

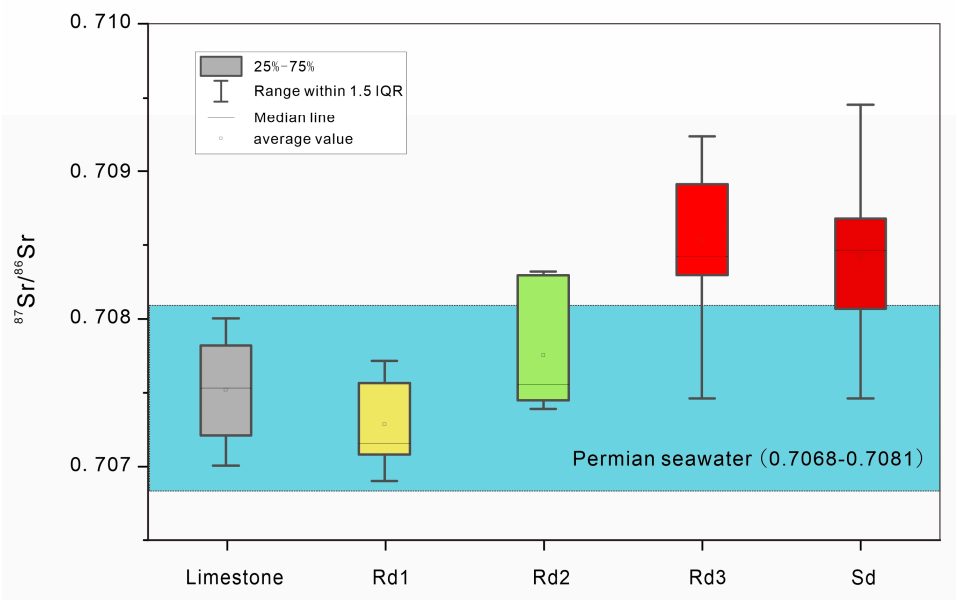


Figure 12. Scatter plots of $\delta^{18}O$ (VPDB) and $\delta^{13}C$ (VPDB) for collected samples in the Middle Permian, middle– to eastern–Sichuan Basin.

5. Discussion

5.1. Diagenetic Sequence

The diagenetic sequence of the three matrix–replaced dolomites (Rd1, Rd2, Rd3) and types of cement (Sd, Cc, Qz) is mainly determined by their paragenesis, crystal characteristics, and inter–relationships.

Rd1 primarily occurs in an incomplete dolomitization form in host limestones (Figure 3) and replaced the mud–crystal matrix preferentially. This is consistent with the formation of dolomite seed crystals during the initial stage of dolomitization of mud [40]. Thus, it is indicated that Rd1 formed during the initial stages of dolomitization. Additionally, some Rd1 samples exhibit fine–to–medium crystal characteristics, which suggest that they have undergone recrystallization of fine–to–medium crystal Rd1. Similarly, remnants of Rd1 are visible in the dirtier central part of Rd2, also suggesting the recrystallization of Rd1 to Rd2 (Figure 4a). Furthermore, Rd2 with fine to medium planar to curved crystals evolved into Rd3 with non–planar medium to coarse crystals (Figure 5a), indicating that Rd3 was formed after Rd2.

The non–planar morphology and strong undulatory extinction of Rd3 suggest that it was formed at a higher temperature exceeding the critical roughening temperature (CRT) [41–43]. Sd commonly occurs as rim cement in the pores/fractures of Rd2 and Rd3, indicating its later formation than Rd2 and Rd3 (Figure 2g–i). Therefore, the continuous growth of Rd1, Rd2, Rd3, and Sd from matrix to pores (Figure 5g,h) suggests a recrystallization process of Rd1 to Rd3 and a precipitation process of Sd [1,44,45]. Furthermore, Rd2 was formed during the shallow burial stage, evidenced by the Rd2 crystals crosscut by stylolites (Figure 4b) [46,47].

Cc and Qz filling in the fractures, especially in Sd, indicate that their formation occurred later than all phases of dolomitization (Figures 2e and 5c,d). In addition, hydrothermal minerals, including fluorite, pyrite, and siderite, are observed to fill the voids in the pore space of Rd2, Rd3, and Sd (Figure 6). Therefore, the mineral formation sequence in the middle Permian dolomite of the study area can be ordered from early to late as follows: Rd1, Rd2, Rd3, Sd, Cc, Qz, and various hydrothermal minerals.

5.2. Sources of Dolomitizing Fluids

Several petrological and geochemical indicators suggest that the dolomitization fluids responsible for the formation of Rd1 were derived from preserved Permian seawater in the strata. The $^{87}Sr/^{86}Sr$ ratios of Rd1, which fall within the distribution range of the contemporaneous seawater $^{87}Sr/^{86}Sr$ ratios during the Permian (0.7068–0.7081), indicating that the dolomitization fluids of Rd1 were primarily derived from coeval seawater (Figure 12). Therefore, it is concluded that Rd1 was formed from dolomitizing fluids derived from preserved Permian seawater in the sedimentary sequence.

Multiple pieces of evidence suggest that the dolomitizing fluid responsible for the formation of Rd2 was mainly derived from Permian seawater, and it may have incorporated a minor component of externally–derived hydrothermal fluids. The $\delta^{13}C$ values of Rd2 exhibit consistency with those of Rd1 and the host limestones, indicating the inheritance of their carbon sources. Moreover, Rd2 and limestones exhibit similar REE distribution patterns characterized by relatively flat curves (Figure 9a,b), suggesting a consanguineous nature of their mineralizing fluids [48,49]. The lack of obvious Eu and Ce anomalies further suggests that the diagenetic fluids did not experience a deeply buried reducing environment [50,51]. However, some Rd2 samples exhibit $^{87}Sr/^{86}Sr$ ratios higher than the range of the Permian seawater (Figure 12), indicating that some external fluids may have participated in the water–rock process. The formation of Rd2 is considered to be in shallow burial environments (<500 m) due to the crosscut of stylolites through Rd2 (Figure 4a). Similarly, the Sr contents in Rd2 are significantly lower than those in the limestone samples but markedly higher than those commonly observed in deeply buried limestones [52,53], indicating shallow burial diagenesis. This is because Sr is easily released from the crystal lattice due to its chemical bonding type and electronegativity characteristics that are similar to Ca but different from Mg during the diagenetic process of progressive burial [54].

The fluid inclusions in the clear rims of Rd2 exhibit a uniform temperature range of 83 to 134 °C (average 109.4 °C), which is significantly higher than the temperature calculated based on the maximum shallow–burial depth (i.e., 500 m), confirming that the formation temperature of its diagenetic fluid was extremely high. In addition, the more negative $\delta^{18}O$ values than those of Rd1 (Figure 11) also indicate that the formation temperature of Rd2 was higher than that of Rd1. It is worth noting that the salinity range of the Rd2 inclusions, calculated based on T_{m-ice}, is slightly higher than that of the Permian seawater (4.4 wt%, [55,56]), suggesting that the contribution of external high–temperature and high–salinity fluids to the diagenetic fluid of Rd2 was not significant. The high temperature of the dolomitizing fluids of Rd2 may be influenced by ancient heat flow and geothermal gradient uplift [7], and in turn, the high geothermal gradient could favor the recrystallization of dolomite to form larger crystals of Rd2 [7]. Therefore, the dolomitizing fluid of Rd2 was primarily derived from the Permian seawater within the shallow–burial strata, mixing with a small portion of external hydrothermal fluids with high temperature, salinity, and $^{87}Sr/^{86}Sr$ ratio.

The Rd3 and Sd are primarily composed of high–temperature, high–salinity brines from the deep basin, and Permian seawater also contributed to their formation. The large and curved crystals observed in these samples indicate rapid crystal growth and high formation temperatures [41,43]. The $\delta^{13}C$ values of the samples are consistent with the host limestone, suggesting that the carbon source is inherited.

The $^{87}Sr/^{86}Sr$ ratios of most Rd3 and Sd samples are higher than those of the contemporaneous Permian seawater and other types of dolomites, indicating the possible influence of either higher degrees of evaporation [57,58] or large–scale water–rock interaction with external fluids with high $^{87}Sr/^{86}Sr$ ratios [59,60]. However, the sedimentary environment in the study area during the Middle Permian period was a broad carbonate platform [61,62], and there is no evidence of evaporite minerals, indicating a lack of evaporation. Therefore, the most likely cause of the high $^{87}Sr/^{86}Sr$ ratios of the Rd3 and Sd is the second scenario, where the influx of a large volume of external fluids with high $^{87}Sr/^{86}Sr$ ratios leads to this feature. The increase in the $^{87}Sr/^{86}Sr$ ratio results from the infiltration of hydrothermal

fluids enriched in ^{87}Sr from clastic rock strata of the basin into the diagenetic fluids (*e.g.*, those from the lower Silurian and Ordovician strata; [12]), with the basement faults serving as the conduit for the fluids [45,63,64].

Moreover, the high homogenization temperatures and salinities of the fluid inclusions in Rd3 and Sd further support this conclusion (Figure 8). Additionally, the positive Eu anomalies also indicate that the diagenetic fluids in Rd3 and Sd experienced a deep reducing environment (Figures 9c,d and 10d) [65]. Compared to the host limestones, Rd3 and Sd samples exhibit a significant increase in Mn content (Figure 10c), which is the result of the input from external fluids. The Mn content variation is also reflected in the strong luminescence of Rd3 and Sd (Figure 5) [66,67]. The Sr content of Rd3 is relatively lower than that of Rd2 because Sr is continuously lost with increasing dolomitization [68,69]. Furthermore, it is found that hydrothermal minerals, including fluorite and siderite, are filled within crystals of Rd3 and Sd (Figure 6d–f), indicating that the high–temperature and high–salinity fluid is hydrothermal fluid [1,9], as these mineral assemblages are products of hydrothermal activity.

Therefore, the high temperature, high salinity, and significantly positive Eu anomaly provide evidence that the fluid responsible for the dolomitization of Rd3 and Sd was mainly derived from hydrothermal fluids, which penetrated through the high–^{87}Sr–bearing clastic strata before entering the Middle Permian through deep faults. However, the presence of inherited carbon sources and the $^{87}Sr/^{86}Sr$ ratios of a small portion of the samples falling within the range of Permian seawater also suggest that residual seawater in the strata contributed to the formation of Rd3 and Sd.

5.3. Genetic Mechanism of the Dolomites

Based on the above analysis, the diagenetic fluids of the dolomites in the Middle Permian of the central Sichuan Basin are mainly derived from seawater and deep–seated hydrothermal fluids. The heterogeneity in the formation and spatial distribution of different types of dolomites resulted from the degree of involvement of different source fluids, hydrological circulation patterns, and differences in water–rock interactions in different stages of diagenesis. Considering the sedimentary characteristics, tectonic activity, burial characteristics, and paleotemperature characteristics of the central Sichuan Basin comprehensively, we propose that the genetic mechanism of the Middle Permian dolomites is the result of seawater–hydrothermal mixed dolomitization caused by ELIP activity.

Rd1 might be formed as the primary mineral along the calcite in the original seawater. The high mud content could facilitate the growth of primary dolomite through mechanisms of clay surface–induced dolomite formation. The low Mn in the limestone associated with Rd1 also indicates weak diagenesis. On the other hand, the conversion of aragonite to calcite in early seawater may be responsible for the higher Sr concentration in limestone (Figure 10).

The genetic mechanism of Rd2 is interpreted as heated seawater dolomitization under shallow burial conditions. The dolomite seeds that emerged during the Rd1 phase are considered a critical constituent for the dolomitization process of Rd2. Additionally, the pre–and post–eruption periods of the ELIP led to a relatively high geothermal temperature that facilitated the extensive development of Rd2. The anomalous temperature rise was initiated by the thermal energy emanating from ELIP, which commenced at 290 Ma and terminated at 240 Ma [22]. Correspondingly, it has been confirmed that the formation time of the main types of Middle Permian dolomite in the central Sichuan Basin is mainly between 251 $\pm$ 11 Ma to 264 $\pm$ 10 Ma, which coincides with the time of ELIP activity, based on the existing U–Pb dating from the Maokou Formation in the southeastern Sichuan Basin [12].

The petrological and geochemical properties of the dolomite in the study area are similar to the aforementioned region of [12], and Rd2 is believed to be of shallow–burial and heated–seawater origin. Therefore, it is believed that the dolomitization in the study area was influenced by the ELIP activity. The activity of the ELIP mantle plume has caused

the reactivation of a series of NE–SW basement faults in the central Sichuan Basin [30,31], providing pathways for the upward migration of deep hydrothermal fluids during the eruption period. Therefore, the Middle Permian strata in the central Sichuan Basin have been in a high paleotemperature environment for a long time, with a paleo–heat flow value as high as 130 mW/m^2, due to the strong thermal effect of the ELIP [22,23].

As ELIP activity reached its peak, the intrusion of magma intensified deep–seated hydrothermal activity in the study area, and the exceptionally high thermal effect and pressure provided the driving force for the upward movement of deep hydrothermal fluids [70]. Deep faults and their associated fracture systems provided preferential pathways for the upward migration of hydrothermal fluids. High–temperature, high–salinity hydrothermal fluids rose to the shallow–buried Middle Permian strata and were released into the formation water (i.e., mainly remained coeval seawater) system. In addition, the extensive karstification caused by the uplift of the study area prior to the ELIP eruption formed many dissolution pores and fractures in the topmost Maokou Formation [26–29]. The basement faults and the dissolution caves and fractures provided pathways for communication between the deep hydrothermal fluids and the overlying seawater in the sedimentary strata, thus facilitating the mixing dolomitization of seawater and hydrothermal [7].

This seawater–hydrothermal mixed fluid circulated constantly in the high–permeability shoal facies of the Middle Permian strata, which were still shallowly buried. The continuous supply of seawater sources provided sufficient Mg^{2+}, and the influx of hydrothermal fluids and the exceptionally high geothermal gradient provided high temperatures to break through the kinetic barrier of dolomitization [71]. Therefore, a large amount of Rd3 and Sd formed near the faults in this stage. Numerical simulation studies [72] have also confirmed that the mixing fluid moves, which is communicated through the basement faults, and can thus meet the Mg flux requirements for large–scale dolomitization and form dolomite along high–permeability fault systems. In addition, dolomitization has a selective nature in the vertical direction, and the mixed fluid of seawater and hydrothermal fluid preferentially migrates and circulates laterally along high–permeability strata near faults [7,73]. Therefore, the shallow buried Mao2 and upper–Mao3 strata deposited in intra–platform shoals were the preferred choice for injecting dolomitizing fluids and water–rock reaction, followed by the deep burial Qi2 strata. The relatively deeper buried condition led to a higher degree of rock compaction and lower permeability of Qi2 strata compared to that of the Mao2 and upper–Mao3 strata, resulting in less formation of dolomites in the Qi2 member.

However, the Qi2 member was relatively deeper buried and had a higher degree of rock compaction, resulting in lower permeability compared to the Mao2 member and relatively less seawater supply, and thus relatively less dolomite formation.

The petrological and geochemical evidence indicates that the formation of Rd2, Rd3, and Sd was continuous. With the continuous influx of deep hydrothermal fluids, the tectonic–hydrothermal Rd3 dolomite was formed around the fault system, while the seawater–dominated Rd2 dolomite was formed away from the fault. The hydrothermal fluid rose along the basal faults and was released as overpressure fluid, causing hydraulic fracturing on a large scale due to the fluid pressure being much greater than the rock pore fluid pressure [3,11,45,63,64,74,75]. Subsequently, the hydrothermal fluid deposited the Sd dolomite mainly in the fractured cracks and pores, forming zebra–like structures and hydraulic breccias.

The incorporation of deep hydrothermal fluids in the diagenetic fluids caused Rd3 and Sd samples to show more hydrothermal signals (e.g., abnormally high $^{87}Sr/^{86}Sr$ ratios, positive Eu anomalies, high–temperature, high–salinity features, etc.). Meanwhile, the hydrothermal acid dissolution could form large dissolution cavities inside Rd2 and Rd3 [76,77]. Then, Sd, cc, fluorite, siliceous, and other hydrothermal minerals precipitated, filled, and blocked the cavities and fractures. Thus, Rd3 and Sd are mainly distributed around the basement faults and are featured by limited lateral extension due to the massive hydrothermal fluids released from the deep faults.

Excessive recrystallization led to pore blockage, making it difficult for fluids to continue to flow laterally [78–80]. Once complete dolomitization and mineral stabilization have been achieved, even if more magnesium–rich fluids enter the system, the size of the dolomitization body will not increase [3,8,81,82], and Rd3 and Sd would remain concentrated in the faults and fracture networks. In contrast, as hydrothermal fluids migrated laterally in highly permeable beach facies, the proportion of hydrothermal fluids in the formation water system decreased, and more Rd2 was formed at the sites away from the hydrothermal source. This is also the reason why weak hydrothermal signals are reflected in Rd2 (e.g., $^{87}Sr/^{86}Sr$ ratios and salinity slightly higher than Permian seawater). If there were many dense companion faults in the basement fault system, the above dolomitization process could result in the connection of Rd2 largely and extend laterally along high–permeability shoal deposits. Therefore, we suggest a relatively continuous process of the formation of Rd2 to Sd dolomites. This is also supported by the U–Pb dating analysis that the formation of these types of dolomite occurred during the peak of ELIP activity [12].

In summary, the main cause of the formation of Middle Permian dolomites in the central Sichuan Basin is attributed to the seawater–hydrothermal mixing dolomitization via the effects of ELIP activity. Dolomitizing fluid circulation was facilitated by the activation of the basement faults, karst pores in the overlying rock, and anomalous high temperature from deep and shallowly buried high–permeability strata. During the peak of ELIP activity, continuous upwelling of deep hydrothermal fluids resulted in the persistent formation of Rd2, Rd3, and Sd. The dolomitizing fluids of Rd2 consisted mainly of seawater, making it the forefront of the dolomite body. The dolomitizing fluids of Rd3 and Sd, which were dominated by deep hydrothermal fluids, were primarily distributed along the fault system. Excessive dolomitization caused by hydrothermal activity might have inhibited the lateral migration of hydrothermal fluids.

6. Conclusions

1. In the eastern part of the Middle Permian in the Sichuan Basin, dolomites mainly occur in the upper part of the Maokou Formation and the top of the Qixia Formation, consisting mainly of three types of replacive dolomites (Rd1, Rd2, and Rd3) and saddle dolomite cement (Sd).
2. Petrological and geochemical evidence indicates that Rd1 formed during the initial stage of burial, mainly from residual seawater in the strata.
3. Intense hydrothermal activity related to ELIP caused seawater–hydrothermal mixing dolomitization, which was the main cause of the formation of Rd2, Rd3, and Sd. Activated basement faults, freshwater dissolution cavities at the top of the strata, and high–permeability strata were the main pathways for fluid circulation. The diagenetic fluids of Rd3 and Sd contain more deep–seated hydrothermal fluids, reflected in their higher $^{87}Sr/^{86}Sr$ ratios, distinct Eu–positive anomalies, and very high temperature and salinity. Their distribution is also controlled by basement faults.
4. This study provides a good example for investigating the formation mechanism of dolomite controlled by faults under the influence of anomalous thermal effects.

Author Contributions: Investigation, H.T. and J.W.; Resources, B.L.; Data curation, X.Y.; Writing—original draft preparation, H.Z.; Writing—review and editing, J.G. and Y.D.; Visualization, J.W.; Funding acquisition, L.P. and R.L. All authors have read and agreed to the published version of the manuscript.

Funding: This research was funded by SINOPEC Exploration Company, grant number 35450003–21–ZC0607–0003, CSC (grant number 202108505045) and the Innovation and Entrepreneurship Project of Chongqing Jiaotong University (grant number X2022106180).

Data Availability Statement: No new data were created or analyzed in this study. Data sharing is not applicable to this article.

Acknowledgments: Thanks to the University of Barcelona for providing the office space and experimental conditions for the corresponding author and Yunnan University for the fluid inclusion analysis conditions.

Conflicts of Interest: The authors declare no conflict of interest.

References

1. Davies, G.R.; Smith, L.B., Jr. Structurally controlled hydrothermal dolomite reservoir facies: An overview: Reply. *AAPG Bull.* **2007**, *91*, 1342–1344. [CrossRef]
2. Barale, L.; Bertok, C.; Salih Talabani, N.; d'Atri, A.; Martire, L.; Piana, F.; Préat, A.; Hollis, C. Very hot, very shallow hydrothermal dolomitization: An example from the Maritime Alps (north–west Italy–south–east France). *Sedimentology* **2016**, *63*, 2037–2065. [CrossRef]
3. Koeshidayatullah, A.; Corlett, H.; Stacey, J.; Swart, P.K.; Boyce, A.; Hollis, C. Origin and evolution of fault–controlled hydrothermal dolomitization fronts: A new insight. *Earth Planet. Sci. Lett.* **2020**, *541*, 116291. [CrossRef]
4. Lavoie, D.; Chi, G.; Urbatsch, M.; Davis, W.J. Massive dolomitization of a pinnacle reef in the Lower Devonian West Point Formation (Gaspé Peninsula, Quebec): An extreme case of hydrothermal dolomitization through fault–focused circulation of magmatic fluids. *AAPG Bull.* **2010**, *94*, 513–531. [CrossRef]
5. Friedman, G.M. Structurally controlled hydrothermal dolomite reservoir facies: An overview: Discussion. *AAPG Bull.* **2007**, *91*, 1339–1341. [CrossRef]
6. Mansurbeg, H.; Morad, D.; Othman, R.; Morad, S.; Ceriani, A.; Al-Aasm, I.; Kolo, K.; Spirov, P.; Proust, J.N.; Preat, A. Hydrothermal dolomitization of the Bekhme Formation (Upper Cretaceous), Zagros Basin, Kurdistan Region of Iraq: Record of oil migration and degradation. *Sediment. Geol.* **2016**, *341*, 147–162. [CrossRef]
7. Dong, Y.; Chen, H.; Wang, J.; Hou, M.; Xu, S.; Zhu, P.; Zhang, C.; Cui, Y. Thermal convection dolomitization induced by the Emeishan Large Igneous Province. *Mar. Pet. Geol.* **2020**, *116*, 104308. [CrossRef]
8. Koeshidayatullah, A.; Corlett, H.; Stacey, J.; Swart, P.K.; Boyce, A.; Robertson, H.; Whitaker, F.; Hollis, C. Evaluating new fault–controlled hydrothermal dolomitization models: Insights from the Cambrian Dolomite, Western Canadian Sedimentary Basin. *Sedimentology* **2020**, *67*, 2945–2973. [CrossRef]
9. Zheng, H.; Ma, Y.; Chi, G.; Qing, H.; Liu, B.; Zhang, X.; Shen, Y.; Liu, J.; Wang, Y. Stratigraphic and Structural Control on Hydrothermal Dolomitization in the Middle Permian Carbonates, Southwestern Sichuan Basin (China). *Minerals* **2019**, *9*, 32. [CrossRef]
10. Guo, C.; Chen, D.; Qing, H.; Dong, S.; Li, G.; Wang, D.; Qian, Y.; Liu, C. Multiple dolomitization and later hydrothermal alteration on the Upper Cambrian–Lower Ordovician carbonates in the northern Tarim Basin, China. *Mar. Pet. Geol.* **2016**, *72*, 295–316. [CrossRef]
11. Dong, S.; Chen, D.; Qing, H.; Zhou, X.; Wang, D.; Guo, Z.; Jiang, M.; Qian, Y. Hydrothermal alteration of dolostones in the Lower Ordovician, Tarim Basin, NW China: Multiple constraints from petrology, isotope geochemistry and fluid inclusion microthermometry. *Mar. Pet. Geol.* **2013**, *46*, 270–286. [CrossRef]
12. Yang, T.; Azmy, K.; He, Z.; Li, S.; Liu, E.; Wu, S.; Wang, J.; Li, T.; Gao, J. Fault–controlled hydrothermal dolomitization of Middle Permian in southeastern Sichuan Basin, SW China, and its temporal relationship with the Emeishan Large Igneous Province: New insights from multi–geochemical proxies and carbonate U–Pb dating. *Sediment. Geol.* **2022**, *439*, 106215. [CrossRef]
13. Zhang, J.-Q.; Jin, Z.-K.; Zhu, X.-E.; Li, Y.; Guo, Q.-H.; Shi, S.-T. Open thermal convection dolomitization: An example from East Yunnan (China). *Geol. Mag.* **2021**, *158*, 330–348. [CrossRef]
14. Lin, P.; Peng, J.; Zhang, L.; Lan, X.; Wang, J.; Xia, Q.; Xia, J. Characteristics of multiple dolomitizing fluids and the genetic mechanism of dolomite formation in the Permian Qixia Formation, NW Sichuan Basin. *J. Pet. Sci. Eng.* **2022**, *208*, 109749. [CrossRef]
15. Hu, D.; Wang, L.; Huang, R.; Duan, J.; Xu, Z.; Pan, L. Characteristics and main controlling factors of the Middle Permian Maokou dolomite reservoirs in the eastern Sichuan Basin. *Nat. Gas Ind.* **2019**, *39*, 13–21.
16. Tian, J.; Lin, X.; Zhang, X.; Peng, S.; Chenyu, Y.; Shoubing, L.; Liang, X. The genetic mechanism of shoal facies dolomite and its additive effect of Permian Qixia Formation in Sichuan Basin. *Acta Petrol. Sin.* **2014**, *30*, 679–686.
17. Jiang, Q.; Hu, S.; Wang, Z.; Wang, T.; Li, Q.; Zhai, X. Genesis of medium–macro–crystalline dolomite in the Middle Permian of Sichuan Basin. *Oil Gas Geol.* **2014**, *35*, 503–510. [CrossRef]
18. Chen, X.; Zhao, W.; Liu, Y.; Zhou, H.; Jiang, Q. Characteristics and exploration strategy of the Middle Permian hydrothermal dolomite in southwestern Sichuan Basin. *Acta Pet. Sin.* **2013**, *34*, 460–466. [CrossRef]
19. Chen, X.; ZHao, W.; Zhang, L. Discovery and exploration significance of structure–controlled hydrothermal dolomites in the Middle Permian of the central Sichuan Basin. *Acta Pet. Sin.* **2012**, *33*, 562–569. [CrossRef]
20. Qi, L.; Gu, Y.; He, P.; Wang, Z.; Jiang, Y.; Li, S.; Zhou, Y. Hydrothermal dolomitization in the Middle Permian in the Central Sichuan Basin, SW China: Evidence from petrology, geochemistry, and fluid inclusions. *Arab. J. Geosci.* **2021**, *14*, 1–15. [CrossRef]
21. Huang, S.; Li, X.; Huang, K.; Lan, Y.; Jie, L. Authigenic noncarbonate minerals in hydrothermal dolomite of Middle Permian Qixia Formation in the west of Sichuan Basin, China. *J. Chengdu Univ. Technol.* **2012**, *7*, 343–352. [CrossRef]

22. Zhu, C.; Xu, M.; Yuan, Y.; Zhao, Y.; Shan, J.; He, Z.; Tian, Y.; Hu, S. Palaeogeothermal response and record of the effusing of Emeishan basalts in the Sichuan basin. *Chin. Sci. Bull.* **2010**, *55*, 949–956. [CrossRef]
23. Zhu, C.; Xu, M.; Shan, J.; Yuan, Y.; Zhao, Y.; Hu, S. Quantifying the denudations of major tectonic events in Sichuan basin:Constrained by the paleothermal records. *Geol. China* **2009**, *36*, 1268–1277. [CrossRef]
24. Zhu, C.; Hu, S.; Qiu, N.; Jiang, Q.; Rao, S.; Liu, S. Geothermal constraints on Emeishan mantle plume magmatism: Paleotemperature reconstruction of the Sichuan Basin, SW China. *Int. J. Earth Sci.* **2018**, *107*, 71–88. [CrossRef]
25. He, D.; Li, D.; Zhang, G.; Zhao, L.; Fan, C.; Lu, R.; Wen, Z. Formation and evolution of multi–cycle superposed Sichuan Basin, China. *Dizhi Kexue/Chin. J. Geol.* **2011**, *46*, 589–606.
26. Wang, H.-J.; Yang, Z.-R.; Han, B. Superposed evolution of Sichuan Basin and its petroleum accumulation. *Earth Sci. Front.* **2015**, *22*, 161.
27. Xiao, D.; Zhang, B.; Tan, X.; Liu, H.; Xie, J.; Wang, L.; Yang, X.; Ma, T. Discovery of a shoal–controlled karst dolomite reservoir in the Middle Permian Qixia Formation, northwestern Sichuan Basin, Southwest China. *Energy Explor. Exploit.* **2018**, *36*, 686–704. [CrossRef]
28. Xiao, D.; Tan, X.; Xi, A.; Liu, H.; Shan, S.; Xia, J.; Cheng, Y.; Lian, C. An inland facies–controlled eogenetic karst of the carbonate reservoir in the Middle Permian Maokou Formation, southern Sichuan Basin, SW China. *Mar. Pet. Geol.* **2016**, *72*, 218–233. [CrossRef]
29. He, B.; Xu, Y.-G.; Guan, J.-P.; Zhong, Y.-T. Paleokarst on the top of the Maokou Formation: Further evidence for domal crustal uplift prior to the Emeishan flood volcanism. *Lithos* **2010**, *119*, 1–9. [CrossRef]
30. Wang, Z.; Zhao, W.; Li, Z.; Jiang, X.; Jun, L. Role of basement faults in gas accumulation of Xujiahe Formation, Sichuan Basin. *Pet. Explor. Dev.* **2008**, *35*, 541–547. [CrossRef]
31. Xihua, Z.; Cong, C.; Jie, H.; Long, W.; Chen, X.; Shiwei, X.; Zhaolong, G. The discovery of Middle Permian Guangyuan–Bazhong extensional trough in the Sichuan Basin and its petroleum geological significance. *China Pet. Explor.* **2019**, *24*, 466.
32. Xingzhi, W.; Bo, L.I.; Xiyan, Y.; Long, W.E.N.; Liang, X.U.; Shengyang, X.I.E.; Yao, D.U.; Mingyou, F.; Xuefei, Y.; Yaping, W. Characteristics of "Guangyuan–Wangcang" trough during Late Middle Permian and its petroleum geological significance in northern Sichuan Basin, SW China. *Pet. Explor. Dev.* **2021**, *48*, 655–669.
33. Liu, X.; Qiu, N.; Søager, N.; Fu, X.; Liu, R. Geochemistry of Late Permian basalts from boreholes in the Sichuan Basin, SW China: Implications for an extension of the Emeishan large igneous province. *Chem. Geol.* **2022**, *588*, 120636. [CrossRef]
34. Dickson, J. Carbonate identification and genesis as revealed by staining. *J. Sediment. Res.* **1966**, *36*, 491–505. [CrossRef]
35. Pourmand, A.; Dauphas, N.; Ireland, T.J. A novel extraction chromatography and MC–ICP–MS technique for rapid analysis of REE, Sc and Y: Revising CI–chondrite and Post–Archean Australian Shale (PAAS) abundances. *Chem. Geol.* **2012**, *291*, 38–54. [CrossRef]
36. Chi, G. Equations for calculation of NaCl/(NaCl + $CaCl_2$) ratios and salinities from hydrohalite–melting and ice–melting temperatures in the H_2O–NaCl–$CaCl_2$ system. *Acta Petrol. Sin.* **2007**, *23*, 33–37.
37. Steele–MacInnis, M.; Bodnar, R.; Naden, J. Numerical model to determine the composition of H_2O–NaCl–$CaCl_2$ fluid inclusions based on microthermometric and microanalytical data. *Geochim. Et Cosmochim. Acta* **2011**, *75*, 21–40. [CrossRef]
38. Korte, C.; Jasper, T.; Kozur, H.W.; Veizer, J. $^{87}Sr/^{86}Sr$ record of Permian seawater. *Palaeogeogr. Palaeoclimatol. Palaeoecol.* **2006**, *240*, 89–107. [CrossRef]
39. Korte, C.; Kozur, H.W.; Bruckschen, P.; Veizer, J. Strontium isotope evolution of Late Permian and Triassic seawater. *Geochim. Et Cosmochim. Acta* **2003**, *67*, 47–62. [CrossRef]
40. Choquette, P.W.; Hiatt, E.E. Shallow–burial dolomite cement: A major component of many ancient sucrosic dolomites. *Sedimentology* **2008**, *55*, 423–460. [CrossRef]
41. Gregg, J.M.; Sibley, D.F. Epigenetic dolomitization and the origin of xenotopic dolomite texture. *J. Sediment. Res.* **1984**, *54*, 908–931. [CrossRef]
42. Machel, H.G. Concepts and models of dolomitization: A critical reappraisal. *Geol. Soc. Lond. Spec. Publ.* **2004**, *235*, 7–63. [CrossRef]
43. Sibley, D.F.; Gregg, J.M. Classification of dolomite rock textures. *J. Sediment. Res.* **1987**, *57*, 967–975. [CrossRef]
44. Smith, L.B., Jr. Origin and reservoir characteristics of Upper Ordovician Trenton–Black River hydrothermal dolomite reservoirs in New York. *AAPG Bull.* **2006**, *90*, 1691–1718. [CrossRef]
45. Lavoie, D.; Chi, G. Hydrothermal dolomitization in the Lower Silurian La Vieille Formation in northern New Brunswick: Geological context and significance for hydrocarbon exploration. *Bull. Can. Pet. Geol.* **2006**, *54*, 380–395. [CrossRef]
46. Koehn, D.; Renard, F.; Toussaint, R.; Passchier, C. Growth of stylolite teeth patterns depending on normal stress and finite compaction. *Earth Planet. Sci. Lett.* **2007**, *257*, 582–595. [CrossRef]
47. Andrews, L.M.; Railsback, L.B. Controls on stylolite development: Morphologic, lithologic, and temporal evidence from bedding–parallel and transverse stylolites from the US Appalachians. *J. Geol.* **1997**, *105*, 59–73. [CrossRef]
48. Banner, J.L.; Hanson, G.N. Calculation of simultaneous isotopic and trace element variations during water–rock interaction with applications to carbonate diagenesis. *Geochim. Et Cosmochim. Acta* **1990**, *54*, 3123–3137. [CrossRef]
49. Qing, H.; Mountjoy, E.W. Formation of coarsely crystalline, hydrothermal dolomite reservoirs in the Presqu'ile Barrier, Western Canada Sedimentary Basin. *AAPG Bull.* **1994**, *78*, 55–77.
50. Bau, M. Rare–earth element mobility during hydrothermal and metamorphic fluid–rock interaction and the significance of the oxidation state of europium. *Chem. Geol.* **1991**, *93*, 219–230. [CrossRef]

51. Azomani, E.; Azmy, K.; Blamey, N.; Brand, U.; Al-Aasm, I. Origin of Lower Ordovician dolomites in eastern Laurentia: Controls on porosity and implications from geochemistry. *Mar. Pet. Geol.* **2013**, *40*, 99–114. [CrossRef]
52. Mahboubi, A.; Nowrouzi, Z.; Al-Aasm, I.S.; Moussavi-Harami, R.; Mahmudy-Gharaei, M.H. Dolomitization of the Silurian Niur Formation, Tabas block, east central Iran: Fluid flow and dolomite evolution. *Mar. Pet. Geol.* **2016**, *77*, 791–805. [CrossRef]
53. Widodo, R.W.; Laya, J.C. Controls on diagenesis and dolomitization of peritidal facies, Early Cretaceous Lower Edwards Group, central Texas, USA. *Facies* **2017**, *63*, 1–25. [CrossRef]
54. Vahrenkamp, V.C.; Swart, P.K. New distribution coefficient for the incorporation of strontium into dolomite and its implications for the formation of ancient dolomites. *Geology* **1990**, *18*, 387–391. [CrossRef]
55. Horita, J.; Friedman, T.J.; Lazar, B.; Holland, H.D. The composition of Permian seawater. *Geochim. Et Cosmochim. Acta* **1991**, *55*, 417–432. [CrossRef] [PubMed]
56. Lowenstein, T.K.; Timofeeff, M.N.; Kovalevych, V.M.; Horita, J. The major–ion composition of Permian seawater. *Geochim. Et Cosmochim. Acta* **2005**, *69*, 1701–1719. [CrossRef]
57. Mountjoy, E.W.; Machel, H.G.; Green, D.; Duggan, J.; Williams-Jones, A.E. Devonian matrix dolomites and deep burial carbonate cements: A comparison between the Rimbey–Meadowbrook reef trend and the deep basin of west–central Alberta. *Bull. Can. Pet. Geol.* **1999**, *47*, 487–509.
58. Nasir, S.; Al-Saad, H.; Alsayigh, A.; Weidlich, O. Geology and petrology of the Hormuz dolomite, Infra–Cambrian: Implications for the formation of the salt–cored Halul and Shraouh islands, Offshore, State of Qatar. *J. Asian Earth Sci.* **2008**, *33*, 353–365. [CrossRef]
59. Compton, J.; Harris, C.; Thompson, S. Pleistocene dolomite from the Namibian Shelf: High 87Sr/86Sr and δ18O values indicate an evaporative, mixed–water origin. *J. Sediment. Res.* **2001**, *71*, 800–808. [CrossRef]
60. Meyers, W.J.; Lu, F.H.; Zachariah, J.K. Dolomitization by mixed evaporative brines and freshwater, upper Miocene carbonates, Nijar, Spain. *J. Sediment. Res.* **1997**, *67*, 898–912.
61. Li, D.; Chen, H.; Chen, H.; Liang, H.; Peng, C.; Xia, M.; Duan, H. Relationship between reservoir development in the Middle Permian Maokou Formation and paleostructure evolution in the Sichuan Basin. *Oil Gas Geol.* **2016**, *37*, 756–763.
62. Xu, G.; Xie, G.; Long, K.; Song, X. Sedimentary features and exploration targets of Middle Permian reservoirs in the SW Sichuan Basin. *Nat. Gas Ind. B* **2015**, *2*, 415–420. [CrossRef]
63. Davies, G.R.; Smith, L.B., Jr. Structurally controlled hydrothermal dolomite reservoir facies: An overview. *AAPG Bull.* **2006**, *90*, 1641–1690. [CrossRef]
64. Chen, D.; Qing, H.; Yan, X.; Li, H. Hydrothermal venting and basin evolution (Devonian, South China): Constraints from rare earth element geochemistry of chert. *Sediment. Geol.* **2006**, *183*, 203–216. [CrossRef]
65. Hecht, L.; Freiberger, R.; Gilg, H.A.; Grundmann, G.; Kostitsyn, Y.A. Rare earth element and isotope (C, O, Sr) characteristics of hydrothermal carbonates: Genetic implications for dolomite–hosted talc mineralization at Göpfersgrün (Fichtelgebirge, Germany). *Chem. Geol.* **1999**, *155*, 115–130. [CrossRef]
66. Pierson, B.J. The control of cathodoluminescence in dolomite by iron and manganese. *Sedimentology* **1981**, *28*, 601–610. [CrossRef]
67. Machel, H.-G. Cathodoluminescence in calcite and dolomite and its chemical interpretation. *Geosci. Can.* **1985**, *12*.
68. Katz, A.; Matthews, A. The dolomitization of $CaCO_3$: An experimental study at 252–295 °C. *Geochim. Et Cosmochim. Acta* **1977**, *41*, 297–308. [CrossRef]
69. Malone, M.J.; Baker, P.A.; Burns, S.J. Hydrothermal dolomitization and recrystallization of dolomite breccias from the Miocene Monterey Formation, Tepusquet area, California. *J. Sediment. Res.* **1996**, *66*, 976–990.
70. Chi, G.; Xu, D.; Xue, C.; Li, Z.; Ledru, P.; Deng, T.; Wang, Y.; Song, H. Hydrodynamic Links between Shallow and Deep Mineralization Systems and Implications for Deep Mineral Exploration. *Acta Geol. Sin.–Engl. Ed.* **2022**, *96*, 1–25. [CrossRef]
71. Dong, Y. *Genetic Mechanism of the Middle Permian Dolomite in the Sichuan Basin*; Chengdu University of Technology: Chengdu, China, 2020.
72. Benjakul, R.; Hollis, C.; Robertson, H.A.; Sonnenthal, E.L.; Whitaker, F.F. Understanding controls on hydrothermal dolomitisation: Insights from 3D reactive transport modelling of geothermal convection. *Solid Earth* **2020**, *11*, 2439–2461. [CrossRef]
73. Zheng, H.; Wu, J.; Tang, H.; Liu, B.; Yang, X.; Shi, K.; Luo, K.; Qiu, Q.; Dong, Y. Origin of the Multiple–Sourced Cherts in Maokou Carbonates in Sichuan Basin, South China. *Minerals* **2021**, *11*, 1269. [CrossRef]
74. Wendte, J.; Chi, G.; Al–Aasm, I.; Sargent, D. Fault/fracture controlled hydrothermal dolomitization and associated diagenesis of the Upper Devonian Jean Marie Member (Redknife Formation) in the July Lake area of northeastern British Columbia. *Bull. Can. Pet. Geol.* **2009**, *57*, 275–322. [CrossRef]
75. Smith, L.B.; Davies, G.R. Structurally controlled hydrothermal alteration of carbonate reservoirs: Introduction. *AAPG Bull.* **2006**, *90*, 1635–1640. [CrossRef]
76. Yang, H.; Li, K.K.; Pan, W.Q.; Xiao, Z.Y.; Cai, C.F. Burial hydrothermal dissolution fluid activity and its transforming effect on the reservoirs in Ordovician in Central Tarim. *Acta Petrol. Sin.* **2012**, *28*, 783–792.
77. Liu, Q.; Zhu, D.; Jin, Z.; Liu, C.; Zhang, D.; He, Z. Coupled alteration of hydrothermal fluids and thermal sulfate reduction (TSR) in ancient dolomite reservoirs–An example from Sinian Dengying Formation in Sichuan Basin, southern China. *Precambrian Res.* **2016**, *285*, 39–57. [CrossRef]

78. Corbella, M.; Gomez–Rivas, E.; Martín-Martín, J.D.; Stafford, S.; Teixell, A.; Griera, A.; Travé, A.; Cardellach, E.; Salas, R. Insights to controls on dolomitization by means of reactive transport models applied to the Benicàssim case study (Maestrat Basin, eastern Spain). *Pet. Geosci.* **2014**, *20*, 41–54. [CrossRef]
79. Wilson, M.E.; Evans, M.J.; Oxtoby, N.H.; Nas, D.S.; Donnelly, T.; Thirlwall, M. Reservoir quality, textural evolution, and origin of fault–associated dolomites. *AAPG Bull.* **2007**, *91*, 1247–1272. [CrossRef]
80. Sharp, I.; Gillespie, P.; Morsalnezhad, D.; Taberner, C.; Karpuz, R.; Vergés, J.; Horbury, A.; Pickard, N.; Garland, J.; Hunt, D. Stratigraphic architecture and fracture–controlled dolomitization of the Cretaceous Khami and Bangestan groups: An outcrop case study, Zagros Mountains, Iran. *Geol. Soc. Lond. Spec. Publ.* **2010**, *329*, 343–396. [CrossRef]
81. Korneva, I.; Bastesen, E.; Corlett, H.; Eker, A.; Hirani, J.; Hollis, C.; Gawthorpe, R.L.; Rotevatn, A.; Taylor, R. The effects of dolomitization on petrophysical properties and fracture distribution within rift–related carbonates (Hammam Faraun Fault Block, Suez Rift, Egypt). *J. Struct. Geol.* **2018**, *108*, 108–120. [CrossRef]
82. Kaczmarek, S.E.; Sibley, D.F. Direct physical evidence of dolomite recrystallization. *Sedimentology* **2014**, *61*, 1862–1882. [CrossRef]

Disclaimer/Publisher's Note: The statements, opinions and data contained in all publications are solely those of the individual author(s) and contributor(s) and not of MDPI and/or the editor(s). MDPI and/or the editor(s) disclaim responsibility for any injury to people or property resulting from any ideas, methods, instructions or products referred to in the content.